In Situ Measurement of the IceCube DOM Efficiency Factor Using Atmospheric Minimum Ionizing Muons

by

Kulacz, Nicholas

A thesis submitted in partial fulfillment of the requirements for the degree of

Master of Science

Department of Physics

University of Alberta

Abstract

The IceCube Neutrino Observatory is a large scale neutrino detector embedded deep within the Antarctic ice located at the geographical South Pole. It instruments over one cubic kilometre of ice with 5,160 Digital Optical Modules (DOM), each of which houses a 10 inch diameter photomultiplier tube (PMT). Deep in the centre of the detector is a densely instrumented region known as DeepCore which lowers the detection threshold for low energy physics analyses. DOMs in DeepCore contain a PMT with a higher quantum efficiency than the rest of IceCube, resulting in a higher sensitivity to photons. Through the use of the PMTs, IceCube captures Cherenkov light produced by high energy charge particles created in neutrino interactions. Extensive in-lab tests of the DOM's behavior have been done and the characteristics parameterized, but once frozen in the ice, absolute direct in situ calibration is difficult.

Utilizing a sample of atmospheric minimum ionizing muons, selected for their well modeled behavior, charge measurements are compared between the active detector and a Monte Carlo simulation intended to replicate the detector's response. Potential *in situ* effects can cause a discrepancy between the signal response and simulation response. This difference between the real signal and simulation can then be used to construct a scaling factor, the DOM efficiency, to compensate for such effects. By using this method, the DOM efficiency factor that best describes the IceCube DOMs is 0.984 ± 0.023, and for DeepCore DOMs 0.923 ± 0.033, indicating a slight excess of detected charge in simulation.

Preface

The work presented in this thesis is original and is the author's own, except where denoted by citations or mentioned below. The criteria for event selection in chapter 5 was tested and chosen, the considerations discussed in chapter 6 and the conclusions drawn are the author's contribution to this work.

The design, commisioning and operation of the IceCube detector is a product of the effort put fourth by the entire IceCube Collaboration. Development of IceCube specific software used in this thesis is credited to the ongoing work of many colloboration members. Specifically for this work, the development of the in situ measurement is credited to Jake Feintzeig and follow up work to Tania Wood, the simulation use in this work was produced by Sebastian Sanchez using the IceCube framework.

Acknowledgments

Contents

List of Figures

List of Tables

ix

1   Introduction

The Standard Model is the theory used to describe the interactions of particles mediated by the electromagnetic, strong, and weak force [1]. It also classifies all experimentally observed elementary particles, seen in figure 1. The electromagnetic force is mediated through photons and facilitates interactions of photons and electrically charged particles; the strong force is mediated by gluons which are behind the binding of quarks in larger composite particles, hadrons. This leaves the weak force which is mediated by heavy gauge bosons, the $W^{\pm}$ and Z^0, and is the mechanism behind particle decay as well as flavour changing interactions. The neutrino, being the only electrically neutral fundamental fermion, can serve as a fundamental probe into the weak interaction physics explained by the Standard Model.
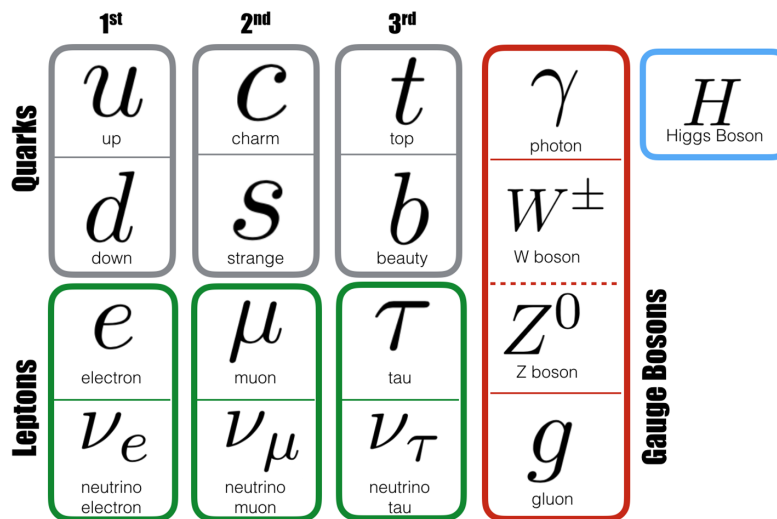
Figure 1: Elementary particles as described by the Standard Model.

1.1 Neutrino Physics

A small, nearly massless neutral particle was first hypothesized by Wolfgang Pauli in 1930 to describe the experimental discrepancy seen in beta decay [2, 3]. Pauli initially referred to this particle as the neutron, which was also the name of the massive neutral particle James Chadwick found in 1932 [4]. The particle Pauli theorized was later coined neutrino, meaning 'little neutral one' in Italian by Enrico Fermi to distinguish the two neutral particles. It was expected the products of a neutron decay, the electron and proton, each had an exact single energy predetermined by the rest mass of the neutron, a feature of a two body decay process. However, experimentally it was observed that the resulting electron did not have the expected single energy, instead it carried a range of energies up to the expected amount. Pauli proposed that this missing energy was being distributed to a neutral particle, one that he could not directly detect, known today as the neutrino.

Neutrinos are electrically neutral leptons each with a distinct flavour corresponding to the charged leptons; electron, muon and tau. Having incredibly light masses, gravitational forces on neutrinos are quite negligible. Only interacting weakly, the neutrino can only exchange weak bosons, resulting in interactions that are usually suppressed given the strength of the weak coupling constant. The type of interaction process depends on the weak mediator, where the exchange of a $W^{\pm}$ is labeled a charged current (CC) interaction and the exchange of a Z^0 is a neutral current interaction (NC). Relevent Feynman diagrams can be seen in figure 2. In CC interactions the incoming neutrino of flavour ℓ exchanges a charge boson and creates a charged lepton of flavour ℓ, if the energy transfer to the target particle is high enough to undergo deep inelastic scattering, it can also result in a hadronic shower full of charged particles. Similarly, in the NC interactions sufficient energy transfer can also create a hadronic

shower in addition to the neutral lepton.

Due to not having electrical or colour charge, neutrinos are able to only interact weakly causing direct detection of the neutrino to be difficult. These reasons, which make the neutrino difficult to detect also enable it to become a powerful messenger to probe astrophysical processes. Not participating in electromagnetic interactions, the neutrino possesses the ability to point back to the source where it was produced. Other conventional cosmic messengers, photons and charged particles, provide valuable information but the former can be absorbed by intersteller debris when traveling extreme distances and the later does not point back to the source due to intergalactic magnetic fields. This means if a neutrino is able to be detected, it can provide a unique source of information describing an interesting astrophysical sources. Recently discovered gravitational waves also enter as a strong messenger for similar reasons to the neutrino and provide another channel of information in astronomy [5].
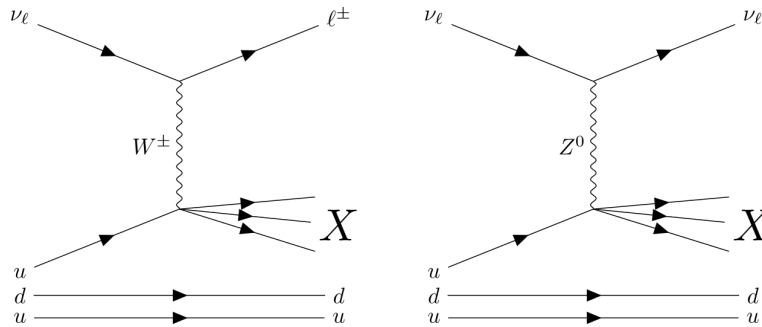
Figure 2: Feynman diagrams of a charged current (left) and neutral current (right) neutrino-proton deep inelastic scattering. Scattering can occur from any valence quark in the proton or neutron, here for example scattering with the up quark. The hadronic shower produced is denoted by X.

1.2 Neutrino Oscillations

The Standard Model describes neutrinos to be exactly massless particles, how-ever neutrino oscillations are an observed phenomena that are directly conflicting with the existence of neutrinos having no mass. This indicates that while the Standard Model is robust, able to describe the majority of particle interactions, there exist gaps in which the theory breaks down. First theorized by Pontecorvo in 1957, based on observations of the neutral kaon being a superposition of two states, that being the K^0 and $\overline{K}^0$ states [6]. This idea, in broad terms, was applied to the neutrino theorizing a superposition of mutiple states. This would allow for the neutrino to oscillate between these states, even in a vacuum. The neutrino flavour states; electron, muon and tau then are not the propagation states, which instead are given by the mass eigenstates labeled 1, 2 and 3. A useful case, one that describes the mixing between ν_μ and ν_τ accurately, is the two flavour oscillation case [7]. The neutrino flavour states, for this case muon and tau, can be given as ν_μ and ν_τ respectively, but propagate in the terms of the mass eigenstates ν_2 and ν_3. Each flavour state can be written as a mixture of the mass states using a unitary matrix, which is able to be written with one single variable, the mixing angle θ,

$$\begin{bmatrix} \nu_\mu \\ \nu_\tau \end{bmatrix} = \begin{bmatrix} \cos\theta & \sin\theta \\ -\sin\theta & \cos\theta \end{bmatrix} \begin{bmatrix} \nu_2 \\ \nu_3 \end{bmatrix}. \tag{1}$$

Given that the mass eigenstates propagate with an exact time dependence, the flavour states can be written as a function of time, taking ν_μ for example as,

$$|\nu_\mu, t\rangle = \cos\theta\, e^{-iE_2 t}|\nu_2\rangle + \sin\theta\, e^{-iE_3 t}|\nu_3\rangle. \tag{2}$$

4

The probability of oscillation of the ν_μ to ν_τ after some time t can be calculated by evaluating

$$P\left(\nu_\mu \to \nu_\tau; t\right) = |\langle \nu_\tau | \nu_\mu, t\rangle|^2 = \left| \cos\theta \sin\theta \, e^{-iE_3 t} \langle \nu_3 | \nu_3 \rangle - \cos\theta \sin\theta \, e^{-iE_2 t} \langle \nu_2 | \nu_2 \rangle \right|^2.$$
(3)

After propagating all the terms and applying Euler's identity as well as several trigonometry identities, the form can be expressed as,

$$P\left(\nu_\mu \to \nu_\tau; t\right) = |\langle \nu_\tau | \nu_\mu, t\rangle|^2 = \sin^2 2\theta \, \sin^2 \left(\frac{E_3 - E_2}{2} t \right).$$
(4)

Assuming the neutrino is highly relativistic such that the neutrino mass is a negligable contribution to its energy, then energy $E \approx$ momentum p using natural units and that time t corresponds to a distance L the probability of oscillating from ν_μ to ν_τ can be written as,

$$P\left(\nu_\mu \to \nu_\tau; L\right) = |\langle \nu_\tau | \nu_\mu, t\rangle|^2 = \sin^2 2\theta \, \sin^2 \left(1.27 \Delta m_{23}^2 \frac{L}{E} \right),$$
(5)

after converting back to physical units. The oscillation probability can be shown depending on two parameters, the mixing angle θ drives the amplitude of oscillation and the squared mass difference Δm_{23}^2, where $\Delta m_{23}^2 = m_2^2 - m_3^2$, drives the frequency of oscillation. The oscillation probability is a function of L/E or the distance traversed over the energy of the neutrino, in this case given in units of km GeV^{-1}. Although this two flavour neutrino case is accurate for this specific circumstance, in reality there are three flavours causing this specialized case to break down. A generalization is then made to move to the three flavour case.

Moving to the theory of three flavour oscillations, now including ν_e, the unitary matrix takes on a 3x3 form to include mixing between three mass eigenstates. The three flavour mixing matrix is known as the PMNS matrix and is given as,

$$
U_{pmns} = \begin{bmatrix} 1 & 0 & 0 \\ 0 & c_{23} & s_{23} \\ 0 & -s_{23} & c_{23} \end{bmatrix} \begin{bmatrix} c_{13} & 0 & s_{13}e^{-i\delta_{CP}} \\ 0 & 1 & 0 \\ -s_{13}e^{i\delta_{CP}} & 0 & c_{13} \end{bmatrix} \begin{bmatrix} c_{12} & s_{12} & 0 \\ -s_{12} & c_{12} & 0 \\ 0 & 0 & 1 \end{bmatrix}, \quad (6)
$$

where c_{ij} and s_{ij} represent $\cos\theta_{ij}$ and $\sin\theta_{ij}$ respectively. The PMNS matrix, in order to be unitary, is fully parameterized by three mixing angles and one complex charge-parity (CP) violating term: $\theta_{12}, \theta_{13}, \theta_{23}$ and δ_{CP}. From global fit parameters it is known that [8],

$$
\theta_{12} = 34.5^{\circ+1.2}_{-1.0}
$$

$$
\theta_{13} = 8.45^{\circ+0.16}_{-0.14}
$$

$$
\theta_{23} = 47.7^{\circ+1.2}_{-1.7}
$$

$$
\Delta m_{21}^2 = 7.55^{+0.20}_{-0.16} \cdot 10^{-5} \text{eV}^2
$$

$$
\Delta m_{23}^2 \approx \Delta m_{13}^2 = 2.50^{+0.03}_{-0.03} \cdot 10^{-3} \text{eV}^2.
$$

Due to the extreme difference in the mixing angles and mass squared terms, the two flavor oscillation special case is a good approximation for the oscillation of ν_μ which allows for the simple oscillation probability given by equation 5 to be valid, stating that all oscillated ν_μ will appear as ν_τ. At this point it is important to note these calculations have only considered oscillations in a vacuum. Specifically, ν_e are able to coherently forward scatter off electrons in matter whereas the other two neutrino flavours cannot.

This introduces a correction to the Hamiltonian dependent on the electron density of the matter being traversed and has been coined the MSW (Mikheyev–Smirnov–Wolfenstein) Effect after those who theorized the effect [9].

1.3 Detection Methods

The first confirmed detection of neutrinos occured in 1956 by the Cowan-Reines experiment [10]. The experiment consisted of two tanks of cadmium chloride dissolved in water surrounded by scintillator in which PMTs were placed. The Savannah River Nuclear Plant was utilized as an electron anti-neutrino source, which possessed a flux over a magnitude higher than any controlled radioactive source. As the neutrinos entered the water tanks, they interacted with protons by undergoing inverse beta decay which resulted in a neutron and positron, the latter annihilated with a surrounding electron and produced photons. The cadmium chloride in the tank acted as an efficient neutron absorber, neutrons produced were captured. The excited cadmium atom then releases a photon 5 μs after the positron signature. The electromagnetic radiation created from the annihilation of the created positron and the delayed neutron signal was detected using PMTs, from which they were able to confirm a neutrino signal above background. Current neutrino detection methods build upon these initial designs but are predominantly classified into two types; radiochemical and Cherenkov, the latter being the central focus.

1.3.1 Radiochemical Detection

Radiochemical detection was theorized by Bruno Pontecorvo, wherein an electron neutrino would strike a chlorine nucleus transforming it into an unstable Argon-37 (halflife $\sim$35 days) atom by converting a neutron into a proton and electron. The argon

would then be harvested from the detector and counted through electron capture and the resulting Auger electron [11]. This method has a low energy threshold of 0.814 MeV, allowing it to measure the electron neutrino flux from the sun. The Homestake experiment set out to do just this, employing Pontecorvo's theory of chlorine detection. With a 380 m^3 tank of tetrachloroethene (C_2Cl_4) 1500 m underground, Raymond Davis Jr. and John N. Bahcall were able to accurately measure the electron neutrino flux emitted from the Sun's nuclear fusion processes [12].

1.3.2 Cherenkov Detection

Cherenkov detection utilizes the charged components of the neutrino interactions to confirm detection. By using a medium with a large index of refraction compared to vacuum, the charged particles created in the interaction will produce Cherenkov light. The production of Cherenkov radiation is analagous to the production of a sonic boom produced by an aircraft traveling faster than the speed of sound. In the case of Cherenkov radiation, a charge particle traverses a dielectric medium faster than the phase velocity of light in that medium. The charged particle excites the surrounding medium as it travels, producing a spherical wave at that point. As the charge particle exceedes the phase velocity of light in the medium, it out paces these spherical waves and from this a shock front is created. The shock front is created at a characteristic angle from the charged particles trajectory, θ_{ch}, corresponding to the index of refraction in the medium given by,

$$\cos\theta_{ch} = \frac{1}{\beta n},\tag{7}$$

where β is the ratio of the speed of the particle to the speed of light in a vacuum and n is the index of refraction of the medium. For extremely relativistic particles this

8

angle is constant, for example in water the Cherenkov angle is approximately 43°. Importantly, the amount of photons produced dN per unit length dx is a function of photon wavelength λ given by,

$$\frac{d^2N}{dxd\lambda} = \frac{2\pi\alpha z^2}{\lambda^2}\left(1 - \frac{1}{\beta^2 n^2(\lambda)}\right),$$ (8)

with α as the fine structure constant, z being the charge of the incident particle, β representing the same quantity in equation 7, and the index of refraction n a function of the wavelength of photon produced [1]. Short wavelength photons dominate the production rate, but is suppressed in ice due to the absorption of ultraviolet photons. Combining the production spectrum with the sensitivity of common PMTs, quantum efficiency peaks at approximately 400 nm wavelength.

Photon detectors, commonly PMTs, can be inserted in the medium and detect the electromagnetic radiation from the neutrino interaction. Many large scale neutrino detectors utilize this method, such as SuperK and SNO, which use a tank of ultrapure water instrumented with PMTs placed on the tanks inner walls [13, 14]. Similarly, experiments can use a natural medium to detect Cherenkov radiation such as ANTARES and IceCube which instrument the Mediterranean Sea and Antarctic ice, respectively [15, 16].

1.3.3 Photomultiplier Tubes

In Cherenkov detectors indirect neutrino detection is carried out by photon detection, and in the case of the experiments mentioned, down to the precision of single photon detection. In order to achieve this level of sensitivity the conventional instrument of choice is the photomultiplier tube. The PMT makes use of a photocathode, a thin layer of a bialkali metal compound possessing a low work function, that when

struck by a photon will eject an electron within the device through the photoelectric effect. The ejected electron is then accelerated towards a chain of dynodes with the use of an incrementally stronger electric field. The dynode is a polished metal electrode that when struck by an electron of sufficient energy will undergo secondary emission resulting in a multiplication of outgoing electrons, known as the gain. Each dynode is held at a strong relative electric potential compared to the previous one, resulting in a cascading amplification of electrons. At the end of the dynode chain the circuit's anode takes in the amplified signal and the corresponding current pulse is measured. Through the use of this technique, single incident photons are amplified to a detectable signal and easily measured. Adjustments to the dynode chain voltage allows for a dynamic gain range, enabling a wide signal range. Noise considerations must be made as any radioactive material present in the device can lead to electron avalanches in the absence of true signal. Dark current is also present as under normal operation the PMT is at extremely high voltages while reading out low current signals, allowing for thermal fluctuations to trigger the readout, leading to launches in the absence of signal. Without perfect insulation, leakage current is able to escape or enter the readout electronics resulting in a potential signal pulse. Timing resolution can also pose an issue for larger PMTs. If the photocathode is large, as is the case with many neutrino experiments, the travel time from the photocathode to the first dynode can be variable resulting in a smearing of the detected signal.

1.4   Charged Particles Through Material

As a charged particle traverses a medium it will lose energy in two dominant electromagnetic processes, ionization of the medium and various radiative losses. These energy loss processes are dependent on the medium being traversed as well as

the charged particle's type and energy. For this study the focus is primarily on muons, as they have relatively low energy losses allowing them to travel appreciable distances in various media. The processes that drive ionization and radiative losses occur in different momentum regimes of the incoming particle, and as such will be discussed separately.

Ionization describes the energy a moving charged particle imparts on nearby electrons pushing them into excited states. Approximating electrons in the medium as being free of external potential fields, the process of heavy charged particles ionizing the medium can be described approximately as Rutherford scattering. This approximation can be adjusted to include the binding energy of the electron in the atom, but atomic effects become negligible at large enough momenta, for example dropping to 1% of the total energy loss for the pion in figure 3 when $\beta = 0.3$.

At low incoming momenta, the energy transfer to the electrons is significantly greater. This is qualitatively described as the charged particle, due to its low velocity, spends more time near the electron allowing it more opportunities to transfer energy to the electron. At these momenta, electrons can no longer be approximated at rest and capture processes become available.

As the charged particle reaches higher energies, radiative losses begin to dominate the total energy loss. This crossover occurs at the particles critical energy, where the bremsstrahlung and pair production, as well as photonuclear interactions to a second order, losses are equal to ionization losses. Bremsstrahlung radiation occurs as the charge particle accelerates through the medium, resulting in the creation of photons and loss of energy. This process has a wide spectrum of energy loss, giving rise to its extremely stochastic nature. With the increased energy loss to photons, pair production becomes another dominating factor as photons annihilate creating positron electron pairs. These energy losses are random, but on average scale linearly with the incoming

11

particle's energy. This stochasticity then leads to largely fluctuations in photon production for a Cherenkov detector, as will be an important characteristic to avoid for this analysis.

At intermediate energies, there lies a minimum stopping power between these two extremes. At low energies the charged particle is able to transfer more energy to the electrons in the medium and at high energies the fractional energy losses are able to reach a much greater maximum. This intermediate energy regime is well described by the Bethe-Bloch equation to an accuracy of a few percent [17]. The stopping power of a charged particle traversing a medium with speed β and Lorentz factor γ can be
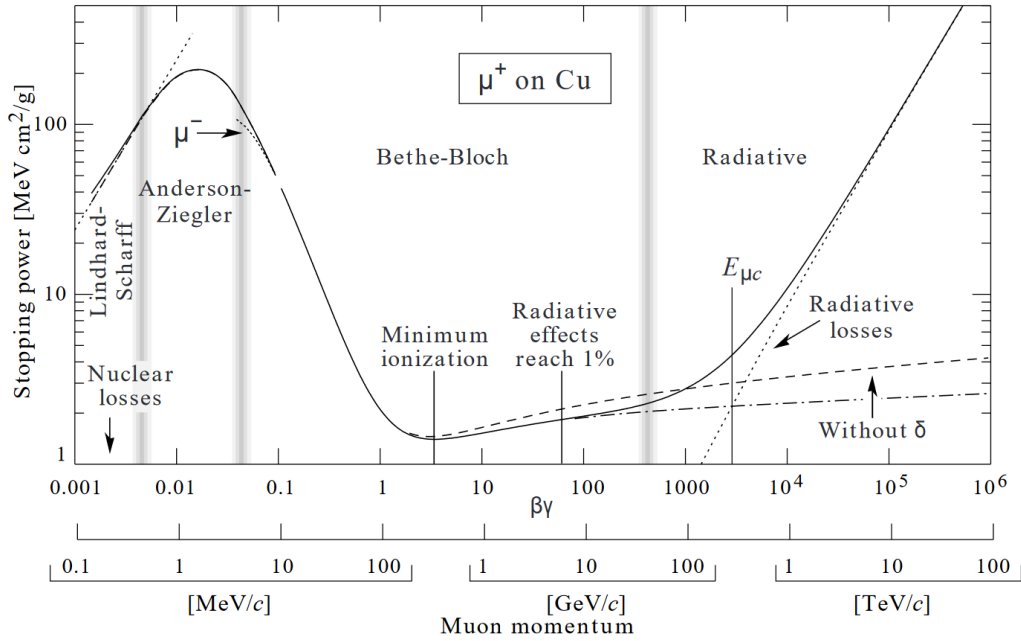
Figure 3: The stopping power of a muon in copper as a function of momentum. These values are averages, the nature of energy deposition is extremely stochastic [1].

expressed as,

$$-\left\langle \frac{dE}{dx} \right\rangle = 4\pi N_A r_e^2 m_e c^2 \frac{Z}{A}\frac{1}{\beta^2}\left[\frac{1}{2}\ln\frac{2m_e c^2 \beta^2 \gamma^2 T_{max}}{I^2} - \beta^2 - \frac{\delta(\beta\gamma)}{2}\right]. \quad (9)$$

Constants in the equation N_A, r_e and m_e refer to Avogado's number, electron radius and mass respectively. T_{max} indicates the maximum energy transfer to an electron while I refers to the mean excitation energy of the medium. A density correction factor δ is introduced to compensate for polarization of the medium as the particle energy becomes extremely high. Importantly the stopping power in the intermediate β region is only a function of β and γ. The Bethe-Bloch formula for muons on copper can be seen in figure 3. This is the region of minimum ionization, where the energy loss of the charged particle is dominated entirely by the ionization of the surrounding medium. Characteristically the energy loss increases logarithmically as a function of incoming particle energy, but are nearly constant when compared to other regions. Due to the near constant nature of this region, these minimum ionizing particles (MIPs) make for good calibration signal events in Cherenkov detectors.

2 IceCube Neutrino Observatory

The IceCube Neutrino Observatory is a Cherenkov detector located at the geographic South Pole in the Antarctic. By utilizing over a cubic kilometre of ice as active medium, it is able to confirm neutrino detection from a wide spectrum of neutrino energies, over six orders of magnitude. The basic detection principle for IceCube is to capture Cherenkov light using photomultiplier tubes housed in Digital Optical Modules (DOMs) which will be discussed in detail.

2.1 Detector

The detector is composed of three targeted sections; IceTop lies on the surface and serves as an air Cherenkov detector, the IceCube array is the main in-ice instrumentation which looks for high energy neutrinos and DeepCore is an infill array located within IceCube that targets low energy neutrinos. A diagram of the detectors components can be seen in figure 4. For this analysis only the IceCube and DeepCore arrays are considered. The primary science goals of the IceCube Neutrino Observatory are to detect astrophysical neutrinos, which has been achieved, as well as expand our knowledge of neutrino and cosmic ray physics.

2.1.1 IceCube Array

The main detector array consists of 86 vertical strings with instrumentation installed between 1450 m and 2450 m beneath the surface. Strings are deployed in a hexagonal pattern with an average lateral spacing of 125 m. Attached to each string in the instrumented region are 60 DOMs which have an equal vertical spacing of 17 m. The horizontal and vertical spacing of these instruments has been optimized to detect
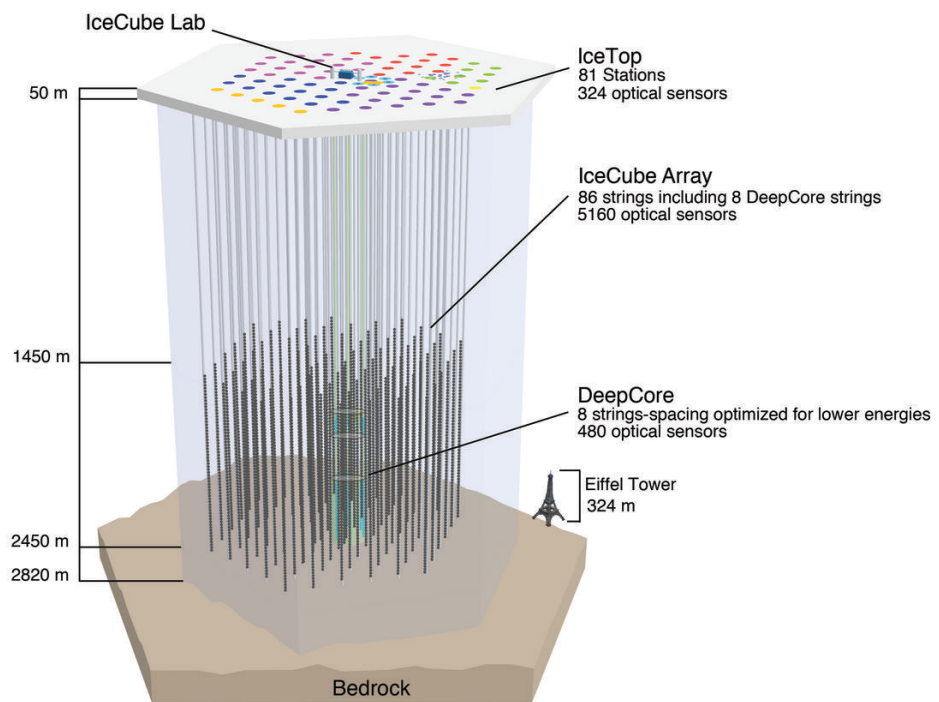
Figure 4: Diagram of full IceCube detector including 86 strings taken from ref. [16].

neutrinos from hundreds of GeV up to energies of PeV.

Due to the active medium being naturally occuring, the properties of the ice are not homogeneous. Located roughly 2000 m to 2100 m below the surface lies a layer of dusty ice that has significantly more scattering and absorption than the surrounding layers [18]. Characterization of these ice properties have been in the past done by stratifying the ice into homogeneous layers, and will be covered in detail in section 2.3.2.

2.1.2 DeepCore

Within the IceCube array there is a more densely instrumented section known as DeepCore. Deepcore lies near the bottom of the main array and specializing in lower energy neutrinos. To achieve this the vertical spacing of the DOMs drop to 7 m and the average lateral string spacing is ∼70 m. Above the dust layer, a section of the detector which is highly concentrated with debris and dust, 10 DOMs are placed to create a veto cap that allows for atmospheric muon rejection. The other 50 DOMs are then located from 2100 m to 2450 m in depth. With this specialized geometry, DeepCore's energy threshold has been sufficiently reduced to see neutrinos on the order of 5 GeV. Notably the DOMs located on DeepCore strings possess a higher quantum efficiency, in lab measurements place the increase at roughly 39% more than the IceCube DOMs [19].

2.1.3 IceTop

The IceTop array works in tandem with the in-ice detector as a source of additional cosmic ray information as well as a useful cosmic ray veto for the in-ice array. The IceTop array consists of 162 water tanks, located roughly above IceCube strings in
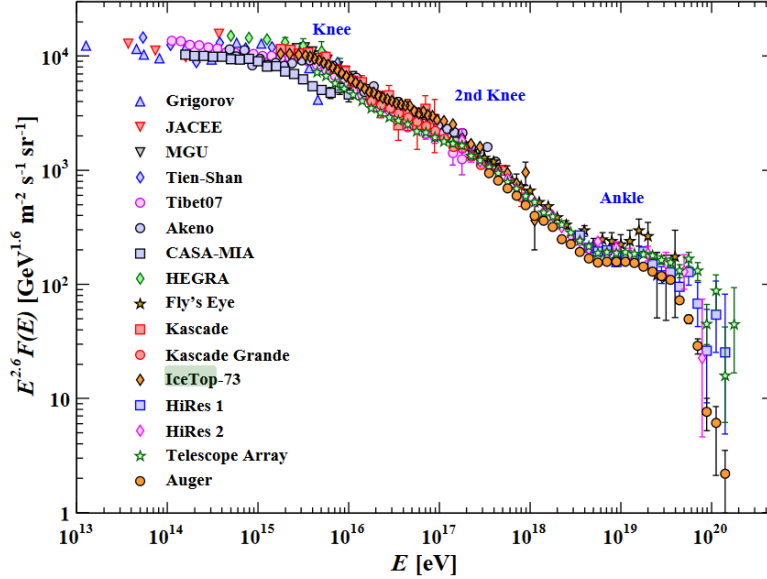
Figure 5: Cosmic ray flux measurements from various experiements. Data from experiments compiled by ref. [1].

pairs. Each pair of tanks is seperated by 10 m. Within each tank two IceCube DOMs are able to detect Cherenkov light, having one DOM set to a high gain and ther other to a low gain. This enables the IceTop array to be sensitive to a wide spectrum of cosmic ray energies. The array has an energy threshold of 100 TeV up to EeV with energy resolution at nearly 8% at the upper end of the spectrum [20]. IceTop is able to probe the "knee" of the cosmic ray spectrum seen in figure 5, a transition in the composition of cosmic ray primaries from protons to heavier nuclei. For the purposes of neutrino physics, the location of IceTop enables strong rejection of downgoing atmospheric muons that could contaminate the detector with neutrino-like events.
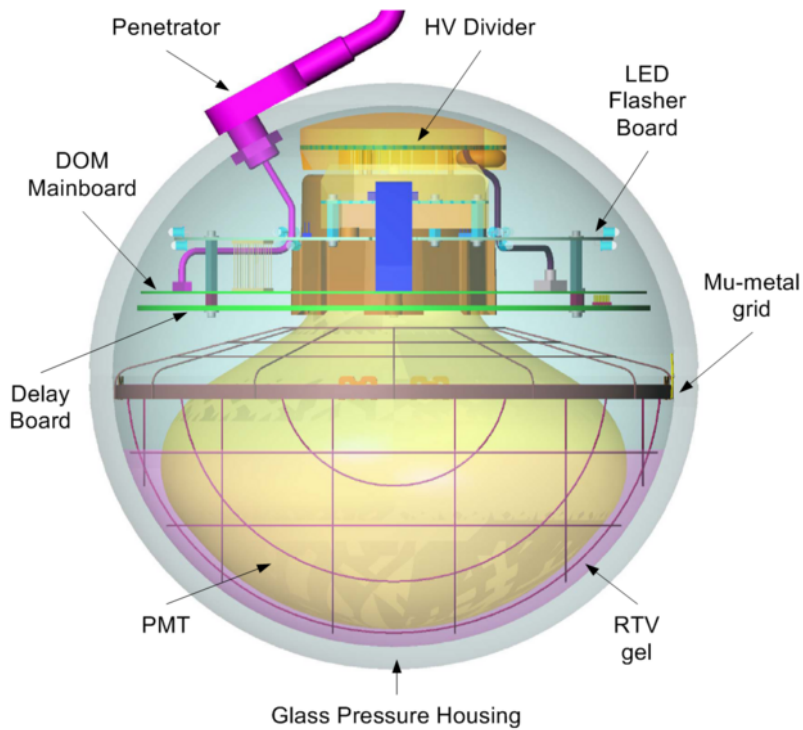
Figure 6: Diagram of Digital Optical Module (DOM) taken from ref. [22].

2.2 Digital Optical Module

The Digital Optical Module is the fundamental data collection and acquisition device for IceCube. The DOM houses a 10 inch diameter R7081-02 PMT designed by Hamamatsu Photonics [21]. Notably the PMT is designed and oriented to only allow sensitivity on the bottom hemisphere of the DOM, optimizing for events coming from deeper in the ice. A diagram of the DOM can be seen in figure 6 and the specifications for this PMT can be seen in table 1. The inactive areas of the DOM hold the electronics required for data acquisition as well as calibration devices to understand the detector better.

18

DOM Characteristic	Specification Value
Spectral response	300 nm to 650 nm
Quantum efficiency at 390 nm	25%
Supply Voltage for gain 10^7	1500 V
Dark rate at -40°C	500 Hz
Transit time spread	3.2 ns
Peak to valley ratio for single photon	2.5
Pulse linearity at 2% deviation	70 mA

Table 1: IceCube DOM specfications as measured in the lab [23].

2.2.1 Data Acquisition

The goal of each DOM is to capture the voltage waveform and the time of detection of each photon in an accurate manner. In order to do this the digitization hardware is located within the DOM where the waveform is read in and sent to a central location. In this system DOM operates independently, so a network is established to ensure correlated DOM observables are properly tagged. Adjacent DOM pairs are connected via a twisted copper wire pair to one another, these then attach to the main cable that relays information to the surface. At the IceCube Laboratory, each string (containing 60 DOMs) feeds information to a DOMHub. The DOMHub consists of eight DOM Readout (DOR) cards, each of which controls eight DOMs. The DOR cards supply power, bootup sequences, code to run, and much of any other DOM operation that must be changed. Importantly the DOR cards also receive information from the IceCube Master Clock which enforces the synchronization of correlated DOM hits. The Master Clock is accurate to within 10 ns over a 24 hour period [22].

A detected photon in the DOM is referred to as a 'hit' which possesses a timestamp and waveform information of the individual event. Waveform information is collected over a period of 6.4 μs which is a conservative time window for relevant charge information from an event in a single DOM, given it takes ~5 μs for light to cross the

19

detector. In order to be a relevant hit, the integrated charge of the waveform must be above the threshold that corresponds to 0.25 of the average single photoelectron (SPE) response. DOM waveform digitization is performed through the use of two distinct digitizers that are located on the DOM mainboard, the Analog Transient Waveform Digitizer (ATWD) and the Fast Analog to Digital Converter (FADC). To accommodate IceCubes large dynamic range, the waveform digitizers target specific types of hits. The ATWD specializes in short, fine grain storage over the first ~420 ns of the hit event, binning the waveform into 128 samples of 3.3 ns. The ATWD takes input from the PMT signal as well as three amplified signals, x16, x2, x0.25, to maintain the dynamic range IceCube observes. Initial conversion applies a x16 amplification to the signal, if this overflows the ATWD then the next channel, x2 amplification, is taken and so on. If the launch has passed the necessary triggers, the waveform is digitized in 29 μs. As the ATWD is unable to record further hits during digitization, two ATWDs reside on the DOM mainboard, alternating digitization, to minimize deadtime. IceCube DOMs maintain a fractional deadtime of 6.6×10^{-5} during high rate periods. Working in conjunction with the ATWD, the FADC utilizes coarser time binning allowing for long waveforms to be digitized where the ATWD would fail at capturing relevant signal. The FADC is a continuous voltage sampler, and when a launch with the proper triggers occurs a 6.4 μs time window is saved and sent to be digitized in 256 samples of 25 ns bins. A dedicated description of the data acquisition is discussed in ref. [22].

Due to the extremely high rate each DOM experiences, certain triggers are enforced to only keep detailed information of interesting events [16]. A common method in IceCube is to flag DOM hits as Hard Local Coincidence (HLC) or Soft Local Coincidence (SLC). When a DOM detects a signal over threshold, it sends a signal to the neighboring four DOMs on the same string, two above and two below. If one of these DOMs made a detection in a ± 1 μs time window the hits are flagged as HLC. SLC hits

20

would be hits that pass threshold but have no coincidence DOMs associated with it. In this case the HLC waveforms are digitized entirely, whereas SLC hits only have the three 25 ns bins digitized. In order to increase the chances of observing a physics relevant signal, these triggers are checked prior to digitization. The signal from the PMT is sent to a single photon electron (SPE) discriminator that checks for accumulated charge of at least 0.25 PE as well as local coincidence hits. The signal is simultaneously sent through a 10 m long copper wire that feeds into the ATWD inputs, delaying the input by approximately 75 ns. If the signal does not meet the threshold or local coincidence checks, digitization can be aborted and the ATWD will rearm for the next hit.

2.2.2 Flasher Board

As well as housing all electronics necessary to preform data acquisition, the DOM mainboard also holds an LED flasher board. This device is able to produce flashes of light allowing for detector properties to be investigated such as electronic response timing, relative DOM positioning, optical properties of the ice and event reconstruction performance [24].

The board holds 12 LEDs that emit at a peak wavelength of 399 ± 14 nm, with two located every 60° around the board. Of the two LEDs at each location, one is oriented to produce horizontal light while the other is oriented to produce light at an upwards angle similar to the Cherenkov angle in ice, 48°. The onboard LEDs have a wide dynamic range allowing yields from 10^6 to 10^{10} photons at rates ranging from 1.2 Hz to 610 Hz. Lab measurements of photon yields show that in a 50 ns pulse, 5.7×10^9 photons are on average produced with an uncertainty up to 20% [25].

2.2.3 High Quantum Efficiency DOMs

As DeepCore was installed after 79 IceCube strings, improvements were made to create DeepCore with a lower energy threshold in mind. Namely the PMT installed in the DeepCore DOMs were built with a different photocathode material resulting in a quantum efficiency that is reportedly 1.39 times higher than the nominal IceCube DOMs [19]. The photocathode was the only change for these DOMs, all other electronics and housing is identicle to standard DOMs. These tests were done in lab at $-45°C$ with a 405 nm source. *In situ* measurements have shown the improvement at 1.35 times that of the nominal DOM. With the higher quantum efficiency, the high quantum efficiency (HQE) DOMs also have a higher dark count rate at 750 Hz. The charge response for a single photoelectron is also slightly shaped differently due to the difference in noise response, showing a more smeared peaked structure as seen in figure 7.

2.3 Characterizing the Detector

In order to do precision measurements with IceCube, the detector itself must be extremely well understood. The advantage of using a natural medium, over a cubic kilometre of active volume, also comes at a price that it is shaped by nature, resulting in inhomogenous ice properties.

2.3.1 Dust Logger

On six IceCube strings, dust loggers were deployed to attempt to characterize the amount of debris present in the ice as a function of depth. The logger uses a 404 nm laser line pointed out horizontally from the bore hole [28]. They are paired with photon
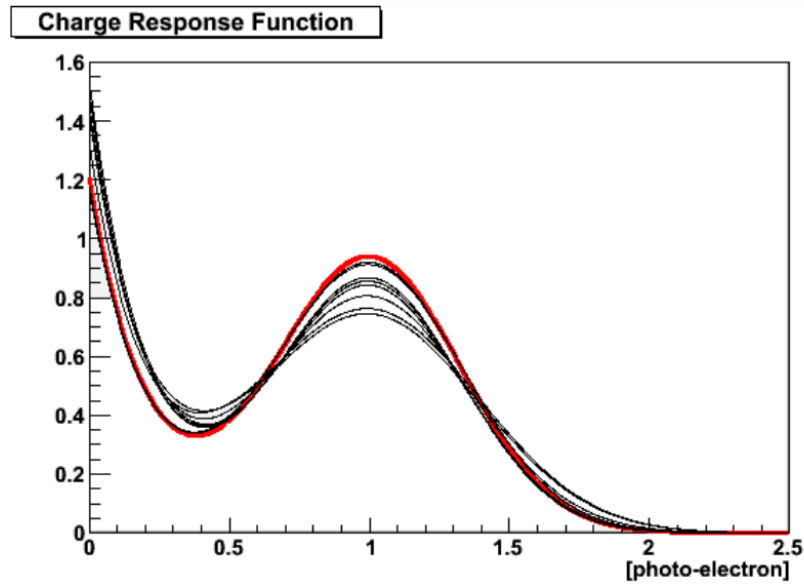
Figure 7: The single photoelectron response for four HQE DOMs (shown in black) compared to the average of 100 standard IceCube DOMs (shown in red) [26].

counters located on the string which will detect scattered photons from bubbles and debris. The dust logger returns information with a spatial resolution on the order of cm, but for absolute depth measurements pressure sensor data was combined to give a resolution of roughly 1 m. This information, combined with subsequent LED flasher runs, provided information of a stratified dust layer formation at the vertical centre of the detector. Dust logger data taken for six IceCube strings is shown in figure 8. Not only was the dust layer characterized, but the bulk ice was shown to have a vertical tilt, indicating that the stratified layers were at an angle with respect to the vertical direction within the detector [29].
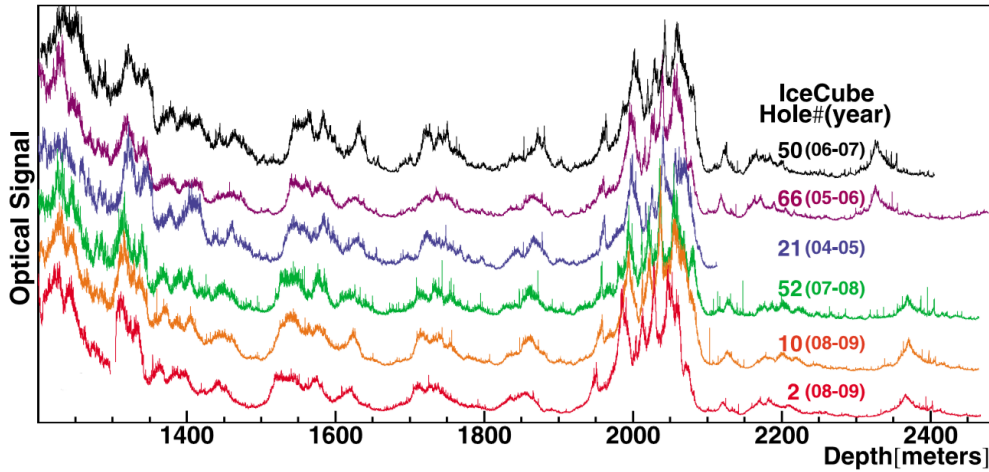
Figure 8: Observed signal using dust logger device on 6 string boreholes [27]. The features of the dust layer, attributed to historical volcanic activity, can be seen around two km below the surface.

2.3.2 Ice Optical Properties

Optical properties of the ice are a crucial component of understanding how the detector operates. These properties are summarized in an ice model, which is a calculated description of the scattering and absorption length as they evolve over the detector [29]. The scattering of photons affect the timing information of the hit, while the absorption of photons affect the overall charge deposition. Developments of the ice model parameterization since IceCube's conception have increased in complexity and detail. By approximating the ice as a stack of stratified homogeneous layers, with layers of common depth having common ice properties, the scattering and absorption has been measured using flasher runs and dust logger data.

In IceCube, the theory of photons scattering on debris in the ice lies in a region between Rayleigh scattering, where the photons wavelength is much greater than the size of the particle, and geometric scattering, where the wavelength is much smaller

24

than the particles being scattered off of. This regime was described by Gustav Mie, and does not possess an analytical general solution [18, 30]. It is calculable by assuming spherical particles, which for the purposes of IceCube, is a sufficient approximation. The scattering angle of a single photon on a piece of debris is highly dependent on the size of debris, which in IceCube ranges from fine grain soot ($\sim$10 nm) to sea salt particles ($\sim$400 nm). Due to dealing with a volume of material, photons will undergo multiple scatters before being absorbed or detected. The absolute scattering length λ_a is a direct measurement of the average length a photon travels before undergoing a single scatter. The value of the average scattering angle $\langle\cos\theta\rangle$ describes the anisotropy of the scattering angle, with $\langle\cos\theta\rangle = 0$ indicating isotropic scattering. Given an absolute scattering length and the average scattering angle the effective length a photon travels after a large number of scatters is given by

$$\lambda_e = \frac{\lambda_a}{1 - \langle\cos\theta\rangle},$$ (10)

as shown in ref. [18]. The parameter λ_e is the effective scattering length, the description for photons that undergo multiple scatters which is the case given IceCube's intrumentation spacing. Mie scatting computational calculations using a 4-component model of the South Pole composition (mineral grain, sea salt, sulfuric acid and soot) show that $\langle\cos\theta\rangle = 0.94$ indicating highly forward scatters [31]. Due to the strong forward peaking, the Henyey-Greenstein approximation is valid to calculate the scattering angle probability function, as it shows consistency with expected scattering effects [18, 32]. The Henyey-Greenstein function was created to describe diffuse scattering interserllar
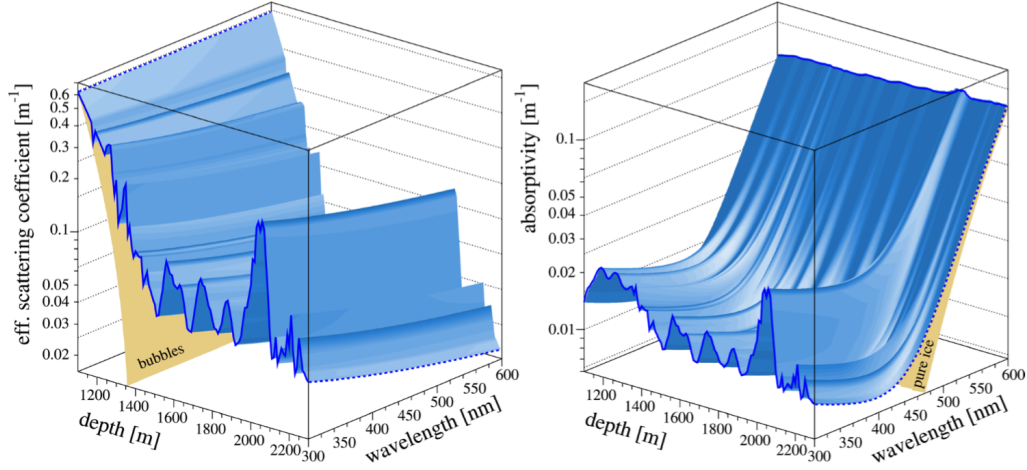
Figure 9: Depth and wavelength dependence of scattering (left) and absorption (right) coefficients, corresponding to inverse scattering and absorption lengths [18].

radiation from dust clouds and follows the form

$$p(\cos\theta) = \frac{1 - \langle\cos\theta\rangle^2}{2(1 + \langle\cos\theta\rangle^2 - 2\langle\cos\theta\rangle\cos\theta)^{\frac{3}{2}}}. \tag{11}$$

This is extremely useful as it can be integrated quite quickly for use in the photon propogation Monte Carlo.

In addition to measuring the scattering length of the ice as a function of depth, the absorption length must also be measured to compensate for loss of photons. For ice, the absorption for wavelengths from 200-500 nm is dominated almost entirely by the content and concentration of debris. Around this region, the ice becomes effectively opaque for detectable photons. Similar to measurements made for the scattering length, the absorption length was measured using unscattered light from LED flashers and pulsed laser sources in the ice. Rather than emitting away from the photon detector, as in the scattering measurement, the light is sent directly at a detector and the

photon survive probability is found and converted to an absorption length. Calculated ice model parameters can be seen visually in figure 9.

All the calculations above assume approximately homogeneous properties in each stratified depth layer, but there are additional parameters that add finer details to the bulk ice properties. The holes for the strings were drilled using a hot-water drill and after instrumentation were refrozen over a period of 24 hours. The refreezing process concentrated all gas in the water into a central column known as 'the bubble column". This column intersects the DOM near the region of highest photon acceptance, resulting in a complex angular acceptance. To experimentally measure this effect, the LED flasher boards are run on a single DOM and the response for that DOM is measured. This allows for photon counting from the six LED pairs equally spaced around the center of the mainboard, giving a description as to where the bubble column is and how much it affects DOM response [24]. The bulk ice also possess birefringence properties due to the shearing of the crystal, essentially elongating the structure along the ice's direction of motion, which has been included in recent ice models [33]. This in turn means photons have different indicies of refraction depending on the direction and polarization they travel with which can lead to incorrect reconstructions. This effect was again measured with the flasher board, showing an average charge variation of 16% per 100 m from source when comparing detection along the axis of anisotropy and perpendicular to it [33]. The ice model is adapted to include new calibration measurements when they are sufficiently understood.

3   Analysis Motivation

This analysis focuses on in situ calibration of the DOM's charge response. Measurements of the single photon electron response have been taken in the lab, but do not precisely match the *in situ* signal. This is due to imperfect models and unknown characteristics of the environment the *in situ* DOMs reside in. Monte Carlo then must take this real effect into account when simulating the DOM response.

3.1   IceCube Physics

IceCube possesses unique instrumentation to probe a wide ranged of physics. While the initial primary goal was to achieve high energy neutrino detection, which has been achieved, the physics applications now are numerous. The dynamic sensitivity of IceCube ranges from as low as 5 GeV to as high as 10 PeV neutrino energy, which overlaps the energy spectrum of astrophysical and atmospheric neutrinos [34]. A few analyses will be covered briefly to demonstrate the significance of energy resolution through the DOM's charge response.

3.1.1   Events In IceCube

There are three types of signal events that IceCube will detect; astrophysical neutrinos produced at an astronomical source, atmospheric neutrinos produced in cosmic rays interacting with the atmosphere and atmospheric muons produced in the same air showers. Events in IceCube have two main topologies, track-line and cascade-like as seen in figure 10. Over the course of a year IceCube expects to detect ∼100 billion atmospheric muons, ∼100,000 atmospheric neutrinos and ∼10 astrophysical neutrinos. In order to veto the enormous background of atmospheric muons, many physics

28

Charged-current ν_μ
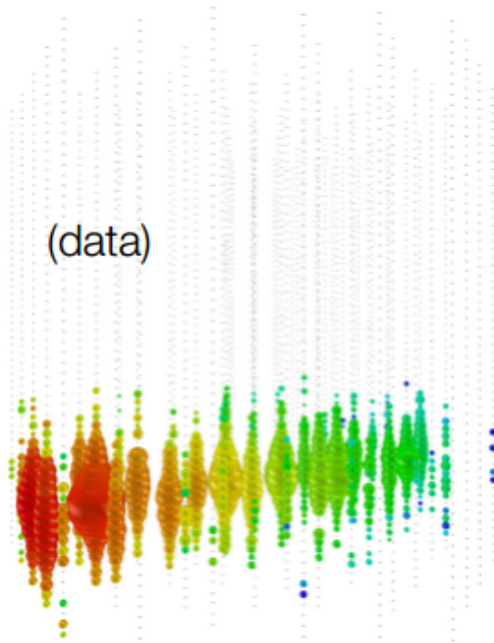
Neutral-current / ν_e
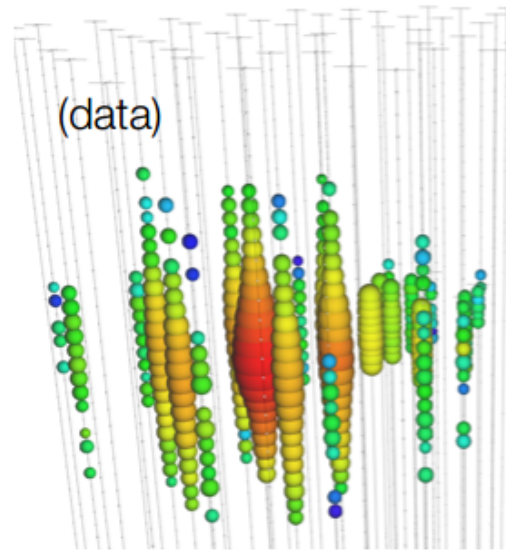
Figure 10: Event topology as seen by IceCube. A charged current ν_μ interaction will result highly energetic muon producing the track-like signature (left). All other interactions produce spherical cascades of light that with the spatial resolution of IceCube are consistent with point sources (right).

analyses will look at events that are directed upwards in the detector, using the Earth to stop muons, as well as events that start within the detector where the first detected light is far from the edges to ensure that it was a neutrino that created the event.

3.1.2 Astrophysical Neutrino Flux Measurement

IceCube, the current largest neutrino detector, is able to make measurements of the astrophysical neutrino flux to energies of several PeV of depositied energy, not normally accessible by other neutrino detectors [36]. The production of astrophysical
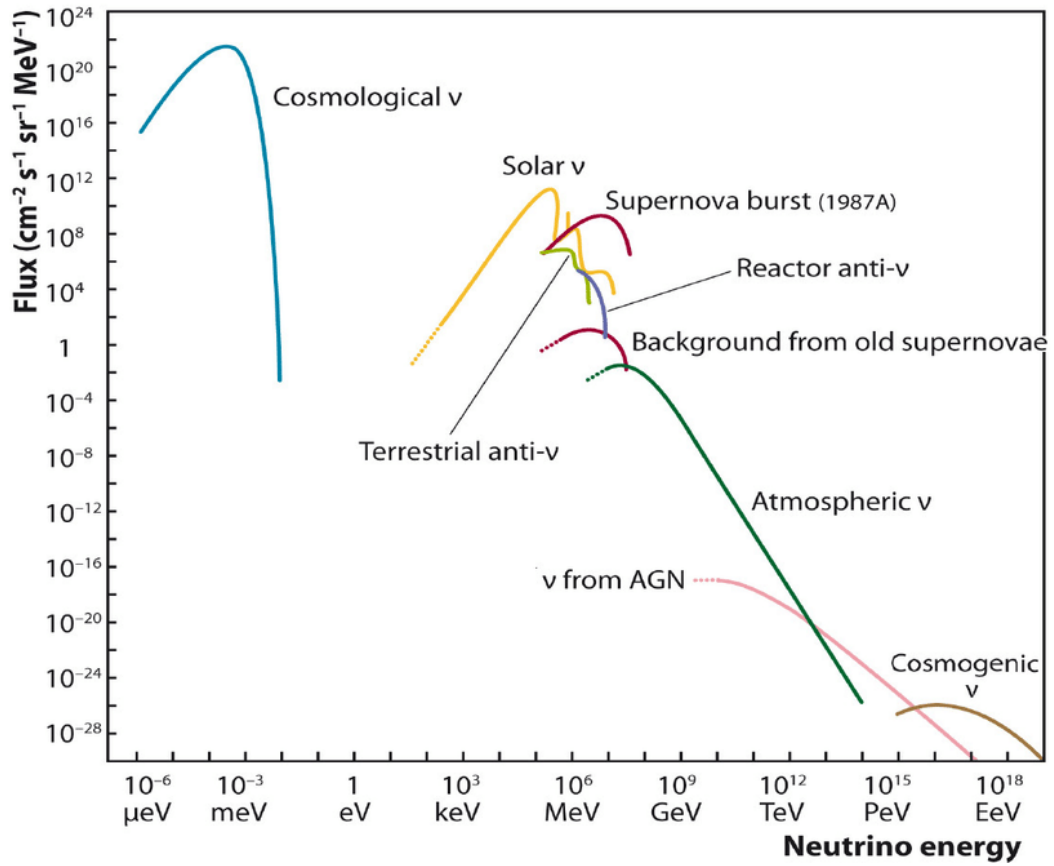
Figure 11: Theory prediction of neutrino flux from sources, taken from [35].

neutrinos is not completely understood, the mechanisms required to produce such energetic events are still a topic of debate. IceCube has recently been able to measure an astrophysical neutrino and, with the help of Fermi-LAT and MAGIC gamma telescopes, direct it back to the blazar it was probably created by, TXS 0506+056, with a significance of 3.5σ [37]. This marks the first detected astrophysical neutrino with confidence to the source of production. In order to make these discoveries, the signal IceCube detects must be filtered to search for events of an astrophysical origin.

Atmospheric neutrinos, neutrinos produced in cosmic ray showers, dominate the neutrino flux in IceCube's low energy range by nearly four orders of magnitude as can be seen in figure 11. Above $\sim$100 TeV the expected atmospheric neutrino flux falls to one event per year, allowing for astrophysical neutrinos, nearly 10 events per year, to be discerned [38]. In addition to the atmospheric neutrinos, atmospheric muons produced in the same cosmic ray shower create a huge background for IceCube. These muons will penetrate the detector from above, leaving tracks of Cherenkov light in the detector. To remove such events, several spatial vetoes are made to the data to remove these muons. A sample known as the High Energy Starting Event sample (HESE) is used to look for events that deposit over 6000 photoelectrons of charge in the enitre detector as well as originate in the centre of the detector indicating it was not a penetrating muon. Data from such an event sample can be viewed in figure 12, where it is compared to theoretical prediction. Neutrino flux measurements in IceCube can then be used to fit a spectral index to the population of astrophysical neutrinos [39, 38]. The spectral index of the astrophysical neutrino flux and flavour composition is then compared to theoretical prediction; possible discrepancies could indicate new production mechanisms, but in the netrino energy range from 25 TeV to 2.8 PeV no deviations from expectation were found [39]. As the spectral index is extremely dependent on the reconstructed energy, with energy resolution of 15% for cascades and a factor of two
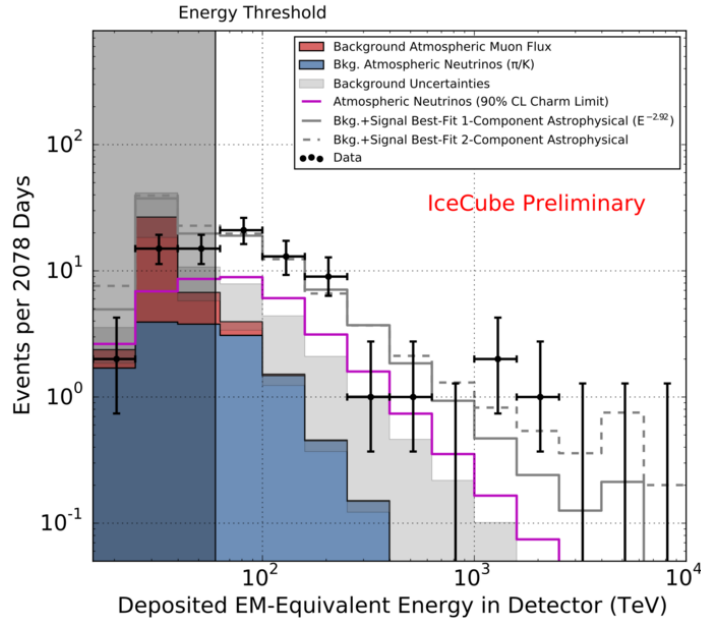
Figure 12: Measured neutrino flux for IceCube with 2078 days of lifetime. Predicted atmospheric flux component is shown as stacked histogram, separated by components. In calculating the spectral index, only events above the energy threshold are considered [41].

in tracks, proper calibration of the detector is paramount to the significance of these claims [40].

3.1.3 Neutrino Oscillations in IceCube

Using the global fit parameters from section 1.2, at L/E $\approx$ 1000 km GeV^{-1} one would expect a large number of ν_μ to oscillate into ν_τ. This can be attainable by observed atmospheric ν_μ with energies ranging from 10-100 GeV. For this reason, the first composite matrix in equation 6 is labeled as the atmospheric sector. IceCube is able to make competitive measurements of Δm_{23}^2 and θ_{23} using atmospheric muon neutrinos [7].
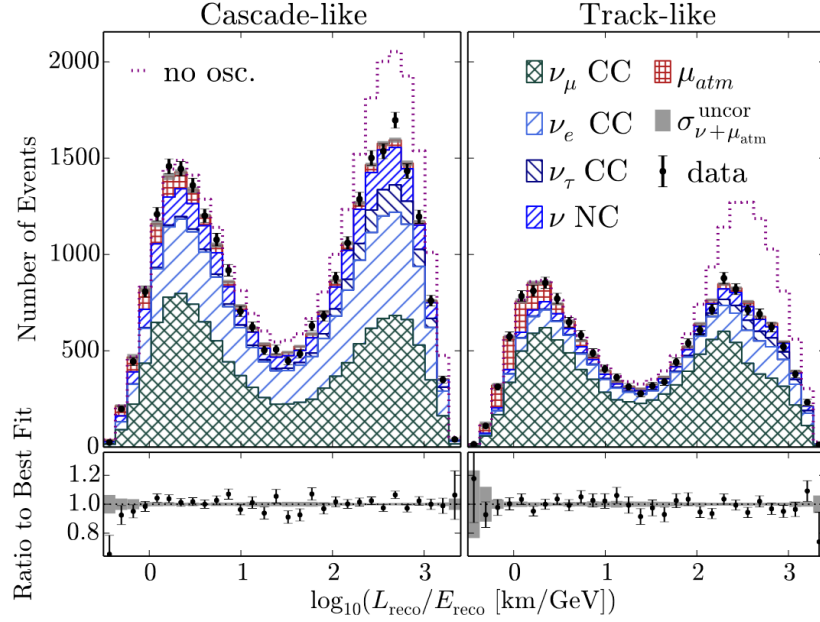
Figure 13: Predicted neutrino flux shown as stacked histogram with consideration of oscillations, each component separated. No oscillation prediction for comparison is shown. Cascade-like and track-like events are separated, with track-like events having a 68% $\nu_{\mu_{CC}}$ purity and cascade-like events having 50% $\nu_{\mu_{CC}}$ purity. Ratio of data to prediction shown below. A full description of the analysis can be found in ref. [42].

IceCube's ability to measure oscillation physics is enhanced greatly by the DeepCore array. With this section of the detector, the energy threshold is lowered from 100 GeV to 5 GeV, giving access to an energy range that maximizes the effect of atmospheric neutrino oscillations through the Earth. By looking for upgoing events in the detector, ones traversing the majority of Earth and thereby reducing the atmospheric muon background significantly, a sample of neutrino events can be collected. By using a two hypothesis likelihood fit, the low energy neutrino sample can be separated into events that look like tracks in the detector (ν_μ charged current) and spherical cascades which encompass all other neutrino interactions. Comparing the flux of ν_μ to theoreti-

cal predictions, the significance of oscillations can be determined as is done in ref. [42]. This comparison can be seen in figure 13. The DOM efficiency parameter enters as one of the larger systematical uncertainties in this analysis, allowing for improvement in the measurement with a tighter constraint on the measured DOM efficiency value.

3.2 DOM Efficiency Factor

The key to accurate energy reconstructions stem from understanding the behavior of the DOMs. The DOMs charge response is linear, until it becomes saturated ($\sim$200 photoelectrons/ns) and charge measurements are no longer linearly correlate to deposited energy [23]. The Cherenkov yield, the expected photon yield as a function of charge particle energy, is $O(10^5)$ photons per every GeV of charged particle energy, which allows for energy calibration in terms of the single photoelectron response [40]. This emphasizes the importance of modeling the single photoelectron response as accurately as possible, as this impacts energy resolution. For example in 2015, a refitting of the single photoelectron response using a more robust approach was done for all the DOMs and a discrepency was found. There was a $\sim$4% higher amount of charge in the single photoelectron response, and upon finding this result, all of IceCube's datum was reprocessed to apply these new templates, correcting the effect [43]. This in turn shifted the total charge of an event to be slightly less than previously thought. This shift in the single photoelectron reponse was a correction applied to data, adjusting what the average charge a single photon would produce. Calibration does not only occur for the real detector but also extends to accurately describe simulation designed to imitate the detector's response.

In a physics analysis a theoretical model that offers some predicted response of the detector is compared to a detected signal. This predicted response of the detec-

tor must then be as accurate as possible to increase confidence in such a comparison. Monte Carlo is used to imitate the detector's response to a specific type of event allowing a comparison to the observed signal. Specifically, the DOM's charge response in simulation should match the real signal for similar events. The PMT's charge response has been measured in the lab, and based on this data a model has been constructed to apply to simulation. In situ effects, however, are not accounted for in this modeling, and as a result of not accounting for such effects, known and unknown, the charge response does not exactly match the in lab measurements the simulation is based on. A scaling factor, the DOM efficiency, is applied to simulation to scale the raw amount of charge observed in a single DOM launch. It is important to stress the DOM efficiency is not the quantum efficiency of the PMT, but rather a factor used to scaled Monte Carlo to be in line with signal. The nominal DOM efficiency of IceCube, previous to this study, is 0.99 ± 0.10. The goals of this analysis is then to more precisely measure this scaling factor. In principle, the method to make this measurement is to compare the Monte Carlo simulated response of an event to a similar event in data and compensate for any inconsistencies.

4   Generated Simulation

This analysis requires the production of several simulated data sets. In general terms four data sets are required for this analysis, each identical except for the simulated DOM efficiency parameter [44]. The overall production chain will be outlined and discussed from generation to analysis ready signal.

4.1   CORSIKA

The production begins with a detailed simulation of extensive particle showers caused by cosmic ray interactions, CORSIKA (COsmic Ray SImulations for KAscade) [45]. CORSIKA was developed by Kascade, a high energy cosmic ray detection experiment. Details of the inner workings of the CORSIKA simulation will not be discussed here but are available in ref. [45]. For IceCube, the default CORSIKA simulation was modified to better suit the needs of the in-ice detector, including propagation steps to go past the surface of the Earth, simplification of cosmic ray composition as well as a more accurate description of horizontal muons incident to the detector [46, 47, 48]. This adapted CORSIKA simulation used, coined dCORSIKA, generated one million cosmic ray shower events according to a 5-component variation of the poly-gonato model [49]. The flux is simplified to only include the five dominant elements that make up the cosmic ray flux; protons, helium, nitrogen, aluminum and iron [50]. The individual components have a different spectral index that is unique to the element.

The simulation's initial step is to interact a high energy nulcei on the atmosphere, then the resulting air shower is propagated down to the depth of IceCube. The energy spectrum of the cosmic rays generated in the simulation follow an $E^{-2.6}$ power law, with a minimum energy of 600 GeV up to a maximum of 100 TeV. The cosmic

rays are generated with an angular distribution from 0°(straight down relative to the detector) to 90°(coming from horizon) isotropically. Events can produce showers that completely miss the IceCube detector, in this case, the event is discarded as no further propagation will result in detection. This simulation, which resembles the background in IceCube, is only interested in the muons that reach the detector. After the muons have crossed a simulated volume, one that extends beyond the detector limits, the muons are sent to PROPOSAL (Propagator with optimal precision and optimized speed for all leptons) [51]. PROPOSAL simulates the energy losses of muon tracks through ionization, bremsstrahlung, photonuclear interactions, electron pair production, etc. covered in section 1.4. IceCube stores the energy loss information of the muon track and passes the information to CLSim, the Cherenkov photon propogator.

4.2   CLSim

CLSim is a simulation package developed to propagate photons through the utilization of OpenCL, a framework that is capable of GPU, as well as CPU, computing[52]. Specifically designed to operate within the IceCube software framework, CLSim propagates simulated Cherenkov photons produced by charged particles or simulated LED photons produced by calibration flashers. To compare, conventional photon propagation for large scale neutrino detectors are based around arrival time distributions from large, interpolated lookup tables. These tables require extensive simulation of photon propagation in order to characterize the entire detector, and as such are difficult to compute, memory expensive and inadaptable to parameter variations in the ice. Tables are generated for the specific model in use, but in systematic studies varying parameters (such as ice models) would result in having to create new lookup tables. Instead CLSim does away with the tables in favour of simulating every photon from a

source until it is either detected or absorbed. This is computational expensive, but by using GPU hardware, the time requirement associated with this cost can come down by over a factor of 100.

CLSim propagates photons by considering the path of a charged particle as a series of small time steps. At each step photons are emitted from the particle's track at the Cherenkov angle and with a random azimuthal angle around the track, the number of photons being sample from a distribution, in CLSim this distribution is a combination of the Cherenkov spectrum and DOM photon acceptance, seen in figure 14, which usually results in the simulation of 0-5 photons per step [52]. The generation of photons can be accessed through parameterized lookup tables generated through extensive GEANT4 simulation of charged particle propagation, the quick choice, or GEANT4 can be used for a full detailed simulation of the charged particle's propagation, passing photons generated to CLSim for propagation, a full review of GEANT4 can be found in ref. [53]. This full detailed simulation allows for information of each individual photon to be saved such as the wavelength, number of scatters, etc. The propagation of the photons is passed to the GPUs which distribute the event out to compute in parallel and then recombine the results into one photon hit series. CLSim convolutes the number of photons emitted by the track, which is peaked to lower wavelengths, with the DOM wavelength acceptance, which has a steep cutoff below ∼300 nm. This resulting distribution forces the generation of fewer low wavelength photons, helping cut computational costs, which then carry a large weight representing that the real number of photons generated at the wavelength. This weight, atypical from the conventional style of weighting, is then used to check if the photon at the DOM is detected through the PMT, with higher weighted photons (ones who represents a large number of unsimulated photons) more likely to be detected. The photon propagation step accounts for detection parameters such as the scattering and absorption length as well as the DOM's

38
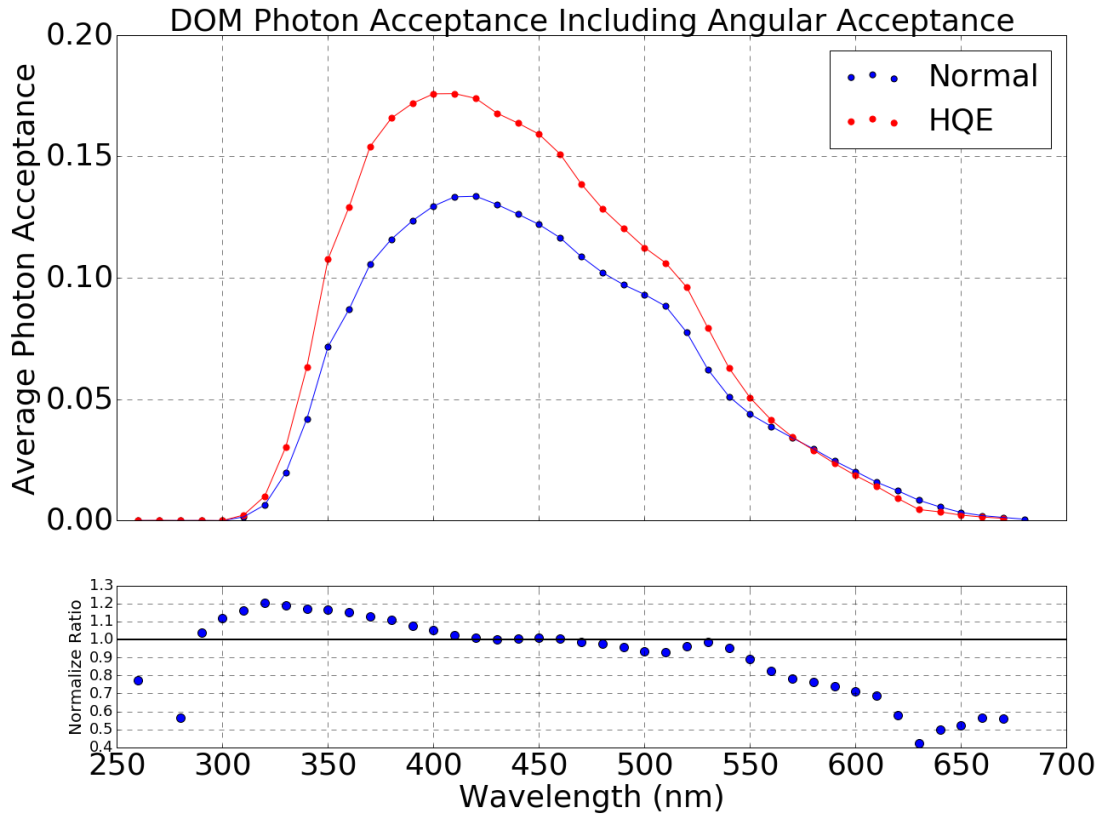
Figure 14: Shown above is the photon acceptance, a combination of the quantum efficiency and angular acceptance, of the IceCube DOM and HQE DOM. These are the distributions used when sampling photon creation in CLSim. In the verison of CLSim used in this analysis, the HQE DOMs were incorrectly modeled, using the exact same distribution of the IceCube DOMs but amplified by the increased QE of 1.35. This error has since been rectified but this analysis uses simulation with the incorrect modeling. The bottom shows the relative difference due to this error in the HQE's photon acceptance.

acceptance [54]. This allows for the parameters of the detector response to be easily varied inbetween simulation sets for different configurations and properties. This flexibility is key to the purpose of this analysis.

For this analysis, CLSim is used to generate four sets of simulations from the initial dCORSIKA simulation. All the CLSim production is identical, except for the DOM efficiency factor. This parameter is used to adjust the effective surface area of the DOMs, thus changing the number of accepted photons, which is identical to the DOM having a correspondingly higher or lower quantum efficiency. For this analysis, the raw number of photons propagated by CLSim was 1.3 times that of the nominal amount. These large number of photons are propagated entirely to the DOM and saved. From this large set, down sampling of the photon hits based on the simulated DOM efficiency parameter, for example at 0.990 (nominal) DOM efficiency factor would save the corresponding fraction of the total DOM hits. At this stage the simulation is split into four sets of varying simulated DOM efficiency. The DOM efficiencies factors used are 90%, 100%, 110%, and 120% of the nominal value, which again is 0.990.

After the photons are entirely propagated, the event has a list of photon arrivals with information pertaining to the photon and DOMs hit. At this stage CLSim uses a model of the DOM's angular acceptance and quantum efficiency to develop a list of Monte Carlo Photoelectrons (MCPE). The MCPE list corresponds to the photons that were able to produce electrons in the PMT, which later on will be turned into pulse signatures.

4.3 Polyplopia

To construct a realistic simulation, coincident background events must be simulated and mapped over signal events. For IceCube, background events are dominanted

by atmospheric muons, the same events in the signal simulation for this analysis. To do this, a separate simulation was developed using the same structure, but without an energy range cut. This simulation set was created solely for background coincidence to the signal sample [55]. The sample is again atmospheric muons, and is simulated through CLSim the exact same as the signal sample.

To overlay the expected background count rate over the signal sample, an Ice-Cube module known as Polyplopia is used [56]. Polyplopia samples from Poissonian distribution to overlay background events onto a sample of signal events. The module will sample from,

$$N(k, \lambda) = \frac{e^{-\lambda}\lambda^k}{k!},$$

(12)

where N is the number of background events to overlay over the signal. λ represents the number of muons entering the detector in a given time interval and k represents the number of coincident showers.

The process of overlaying the events is straightforward. Each signal event samples from this distribution, with no coincidence resulting $\sim$90% of the time [56]. After a signal event has successfully sampled at least one background muon event, the first muon event from the background sample is taken and overlaid onto the signal event, and then is removed from the background sample. In this analysis the overlaying took place after photon propagation, meaning the individual MCPE lists were combined. Alternatively, and more efficienctly, the events could be overlaid at the stage before propagation and then photon propagation would occur simultaneously.

4.4   Detector Simulation

After the final MCPE lists are generated, they have to be processed through the detector response simulation. This piece of the simulation turns the MCPEs into

the expected response the real detector would have to this event. A brief overview of the processes is covered but will not be discussed in depth. Each MCPE represents a photoelectron that is in the PMT, the first stage of the detector simulation is to simulate the PMT's response to this particular photoelectron. From there the DOM's mainboard is simulated and the waveform is digitized from the corresponding photoelectron, complete with threshold and coincidence triggering [57]. In addition to simulating the realistic reponse of the signal photons, noise is also simulated based on a model of the measured noise [58]. The output from the detector simulation is similar to that from the online detector output, ready to be filtered in the Level 2 filter scripts as discussed in section 5.2.

4.5   Weighting

For Monte Carlo events, the spectrum of a specific primary interaction at a specific energy does not correlate to the true spectrum the detector observes. For example, the detector observes a huge quantity of low energy events but the Monte Carlo will only simulate a fraction of this amount. Likewise for extremely high energy primaries the flux small and to lower statistical uncertainty the simulation creates a disproportionally large amount of these types of events. In order to compare the simulation to data, a weight is associated to the event. Take for example a simulation set that is generating primaries,

$$F_{sim}(E, i) = \frac{dN_i}{dAdEd\Omega},$$ (13)

where the fluence, F_{sim}, is the number of primaries of a specific type, i, at a given energy, E, in an area A from a solid angle Ω. The fluence of simulation is integrated over a period of time, known as the effective lifetime of the simulation. This simulated fluence follows some model, various types exist, and usually favouring simulating higher

energy primaries. The expected fluence in a detector is calculated much the same way and will be called, F_{exp}, this is what is truly expected for the detector in a given time.

$$\frac{F_{exp}(E, i)}{dt} = \frac{dN_i}{dt dA dE d\Omega}. \tag{14}$$

The fluence per unit time describes the rate at which particles, differing in type and energy, are incident on the detector. In IceCube the convention to compare these types of events is to calculate a weight for the simulated event, which is calulated by the ratio of F_{exp} to F_{sim},

$$w(E, i) = \frac{F_{exp}}{F_{sim}}, \tag{15}$$

which is the weight of the event in units of s^{-1}. This weight represents, for a specific type and energy, the number of particles the detector will observe in a second. Multiplying this weight by the effective life time of the simulation will result in the number of signal events expected for that type of event. The lifetime of the simulation can be taken as,

$$T_{eff} = \frac{\sum w}{\sum w^2}, \tag{16}$$

which will represent the time the simulation represents in seconds [59]. Using these methods, one could then compare the number of events of a specific type observed in simulation to that observed in detector signal.

5 Event Selection

For this analysis a specific selection of events must be chosen to make the Monte Carlo to data comparison. Specifically, the types of events chosen for this analysis are atmospheric minimum ionizing muons. These events provide the sample with key characteristics that lend itself to measured the DOM efficiency accurately. Firstly and most importantly, minimum ionizing muons lose a near constant amount of energy traversing the ice, as explained in section 1.4. This constant energy loss, being well understood, translates into a constant rate of photon production that is accurately modeled in the simulation. Atmospheric muons also have the benefit of being extremely numerous - over 100 billion trigger the detector a year - as well as producing an easily reconstructable track signature in the detector. To ensure our need for a sample of minimum ionizing muons is met, several levels of analysis cuts are imposed on the signal.

5.1 Analysis Region

This analysis uses a select part of the detector to reduce the impact from potentially uncertain properties of the ice. The ice below the dust layer, which lies approximately across the center (vertically) of the detector, is extremely clear compared to the rest of the detector. The scattering and absorption lengths are favourable in this region, reducing photon detection uncertainty due to ice properties, with the scattering length ∼50 m and the absorption length at ∼140 m. The region encompasses all eight DeepCore strings as well as 18 IceCube strings, allowing for both types of DOMs to be tested and can be viewed in figure 15 and figure 16.
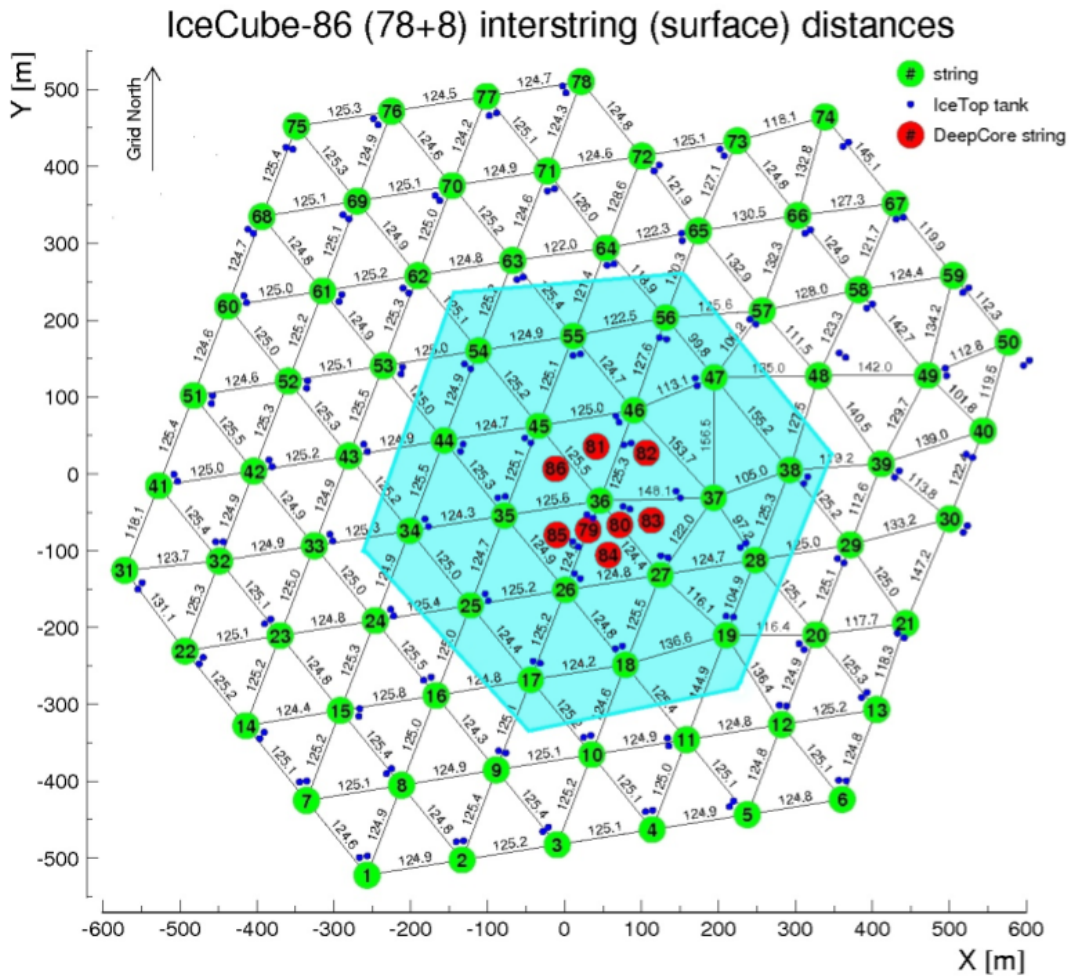
Figure 15: A top view of the analysis region in the shaded cyan area encompassing eight DeepCore strings and 18 IceCube strings.
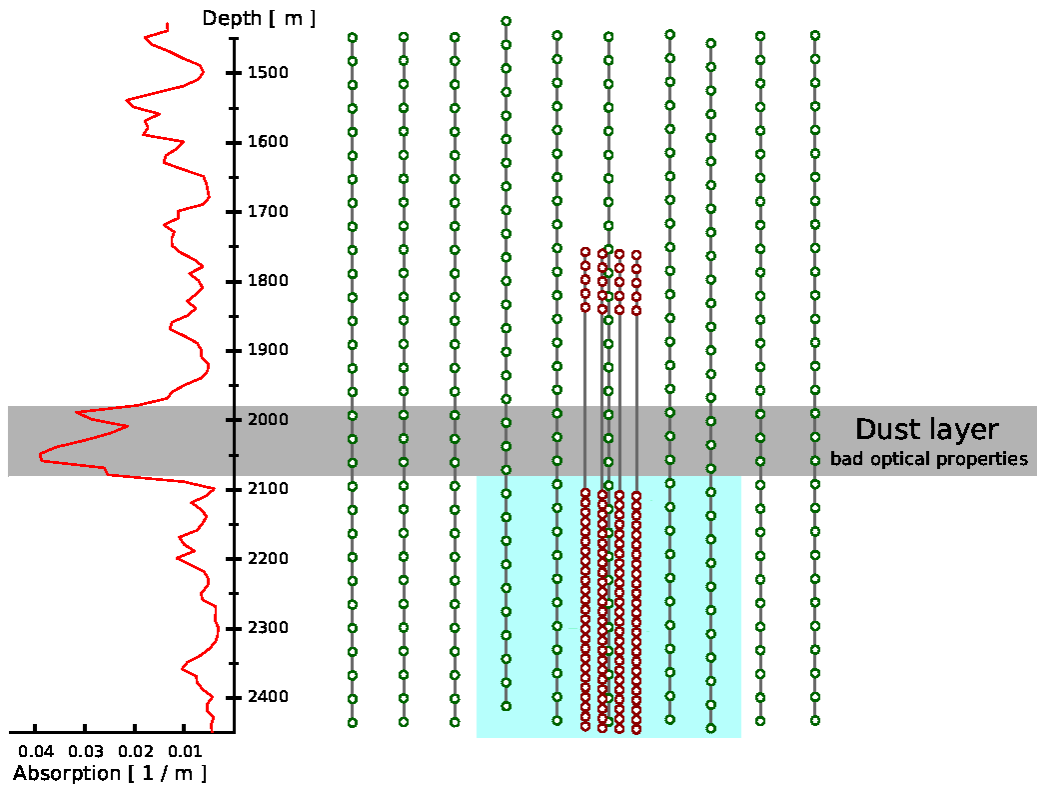
Figure 16: A side view of the anlaysis region (shaded in cyan), displaying the dust layer for reference.

5.2   IceCube Filtering

IceCube processes data online, simultaneously alongside data collection, directly at the pole, applying triggers and filtering in an attempt to preserve only relevant physics events while also operating in the limited bandwidth available (720 kbps per DOM) [16]. As the DOMs launch on a potential event, coincidence is checked in real time, and based on the information exchanged, several triggers can be checked to pass or fail. This analysis is focused on atmospheric muons, which are of little interest to other analyses and as such have no specifically designated trigger. Three triggers are of interest; InIce, SMT8 and MinBias. The InIce trigger simply checks if the event is located within the detector, this is just to separate IceTop events from IceCube events. The SMT8 trigger stands for Simply Multiplicity Trigger with eight counts of coincidence hits. As the DOMs trigger on an event, a 5 µs time window slides alongside the event. When eight HLC (hard local coincidence previously discussed in section 2.2.1) hits are within this window, the SMT8 filter is passed. This allows filtering of events that bear some level of coincidence much higher than a statistical fluctuation of just noise. The last of the data filters used is the MinBias trigger. This trigger is not correlated to any information received from the DOMs, rather it simply chooses random events to pass at a rate of 1/1000. Events in IceCube are saved if any trigger is passed, this means the sample of saved events are biased to include specific types of events related to the trigger. The MinBias trigger is used to save a dataset which has not triggered on any specific types of events, as the events that pass this trigger are completely random. This is particularly useful for this analysis as the majority of these events will be atmospheric muons. In this analysis, all three triggers must be passed to be considered.

47

5.3 Pulse Cleaning

The initial pulse series for a single event contains all the DOMs that fired in the triggered time window. Including every DOM in the series adds noise hits that are undesirable and will potentially cause reconstruction algorithms to fail. Therefore a pulse cleaning algorithm is applied to removed pure noise hits and preserve physics hits. An IceCube algorithm developed by other collaborators, the Radius-Time (RT) cut, looks at a specific DOM which detected charge and creates a distance and time sphere around that DOM. If another pulses is observed in this distance and time sphere then it is allowed into the cleaned pulse series. The chosen distance and time window cuts are 150 m and 1 μs respectively. This is a basic cleaning algorithm, which is then used to construct a more sophisticated cleaning process. Another algorithm developed by collaborators, SeededRT (SRT) cleaning uses the principles in the classic RT cut but is seeded with an already clean series. For example, and in use for this analysis, the SRT cleaning is seeded with the HLC (hard local coincidence) pulses which keeps $\sim$5% of noise hits and $\sim$73% of the signal hits [60]. Using this clean series, the RT cuts are imposed and any addition non-HLC hits that pass the RT cuts are appended to the cleaned series. This process is done iteratively until no changes are made, resulting in a final cleaned pulse series that contains additional information compared to the seeded HLC pulses. Using simulation of common neutrino events, this cleaning method resutls in a pulse series that retains $\sim$6.1% of noise hits and 95% of signal hits [60]. Figure 17 depicts the acceptance and rejection of DOM hits using such an algorithm.

5.4 Event Cuts

The sample after online triggers and filtering is mainly atmospheric muons. Icecube triggers on muons 10^6 times more than neutrinos, but this sample is not yet in
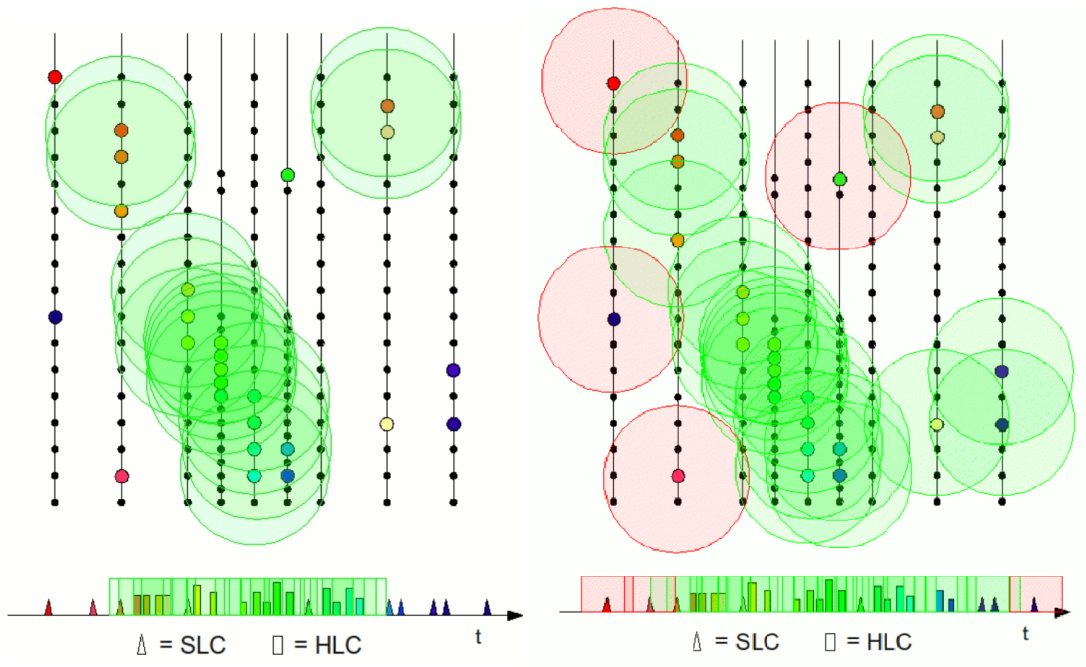
Figure 17: SeededRT pulse cleaning. Left shows the HLC pulses with RT acceptance windows. Right shows the final accepted and rejected DOM hits. Hits within the green region are accepted while those in the red are rejected.

the desired energy range which is below the critical energy of $\sim$1 TeV [61].

5.4.1 Track Reconstruction

The analysis makes use of several track reconstructions in order to recover the incoming muon's direction and potential endpoint. These reconstructions will be listed in terms of complexity, beginning with the most simple.

The first quick reconstruction used to rebuild the incoming muon is LineFit [62]. LineFit serves as the first quick check of the quality of a potential track. Unlike other reconstructions LineFit is a purely deterministic approach and ignores information pertaining to the ice properties, Cherenkov angle with respect to the track and any charge the DOM detected. It uses a simple minimization of the sum of squared distances from the DOM hits to a potential track. While this fit offers little confidence in the true muon's direction, it is primarily used as a seed to feed to a more sophisticated algorithm as a first guess.

The next series of reconstructions are not deterministic, but rather use a likelihood maximization method to find the best fit hypothetical track to explain the data observed [63]. The likelihood function being maximized can have multiple local maxima, which can produce probabilistic results when seeded with an uncertain first guess. The Single Photo Electron Fit (SPEFit) is the next step up from LineFit, and it includes the timing information of the first hit recieved by a triggered DOM into a likelihood maximization. A generalized view of the method used is to estimate a set of parameters $\{\mathbf{A}\}$ for a given set of experimental values $\{\mathbf{x}\}$ by maximizing the likelihood, or probability, of observing data $\{\mathbf{x}\}$ with parameters $\{\mathbf{A}\}$ given by the function,

$$\mathcal{L}(\mathbf{x}|\mathbf{A}) = \prod_i p(x_i|\mathbf{A}), \tag{17}$$

with $p(x_i|\mathbf{A})$ being the probability density function of observing the instance of x_i given the model parameters $\{\mathbf{A}\}$. In practice it is more convenient to find the minimum of the log-likelihood,

$$-\ln \mathcal{L}(\mathbf{x}|\mathbf{A}) = \sum_i \ln \Big(p(x_i|\mathbf{A}) \Big). \qquad (18)$$

To calculate the probability density function $p(x_i|\mathbf{A})$, knowledge of the detection rate of DOMs given any track position and orientation is needed. This could be done through a Monte Carlo driven method, but is computationally expensive. Instead a simplified model is put forth, the Pandel Function [64]. First motivated in the BAIKAL experiment, the probability of a photon reaching a given distance in some expected time was parameterized in the case of an isotropic, monochromatic point source [65]. The exact form will not be discussed here, but it has been shown for IceCube to be consistent with extensive Monte Carlo simulation [66]. Examples of these comparisons can be seen in figure 18. It is also important to note specific parameterization of the likelihood using this Pandel function is dependent on the ice model, requiring new parameterization for new ice models. The next natural extension to the SPEFit method is including all DOM hits into the likelihood fit, called Multiple Photo Electron Fit or MPEFit. This follows nearly the same procedure as SPEFit, but instead of using the first photon arrival time, all arrival times are used.

To achieve higher angular resolution, compared to the Pandel driven methods, the computational expensive tables previously mentioned have been calculated using a Monte Carlo driven method. Using extensive, detailed simulation, tables of discrete values were constructed describing the function $p(x_i|\mathbf{A})$. By having the PDF be constructed specifically for IceCube through simulation, particular effects such as the inhomogeneity of the ice properties and the angular acceptance of the DOMs could be taken into account. These tables have given way to the premier track reconstruction
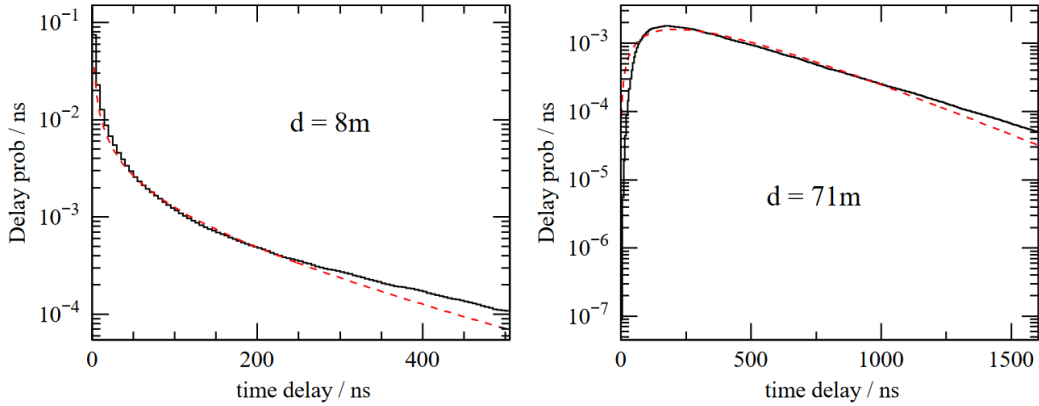
Figure 18: Comparison of time residuals of the DOM using a parameterized Pandel function (dashed) to Monte Carlo simulation for DOMs located at two different distances from a given muon track.

in IceCube, SplineMPE. A combination of the previous MPEFit method, but with using spline tables to construct the probability density function. This ends the reconstructions that identify track-like signatures and emphasize angular resolution. A comparison of the angular resolution of various track reconstructions can be see in figure 19.

The next reconstruction is used to identify what type of muon track the event most likely is: a through-going track, contained track, starting track or stopping track. These classifications refer to the length of the recontructed muon track in the detector, for example a through-going track penetrates the entire detector. The FiniteReco reconstruction specializes in making this classification. This reconstruction also uses a likelihood method, but it focuses on a hit/no-hit probability for the DOMs with a given muon track [67]. The basic principle relies on a potentially stopping muon track to no longer produce light past the point at which the muon truly stops, resulting in DOMs along the infinite track (through-going) hypothesis to show missed hits where they were expected. The reconstruction calculates negative log-likelihood values for

52
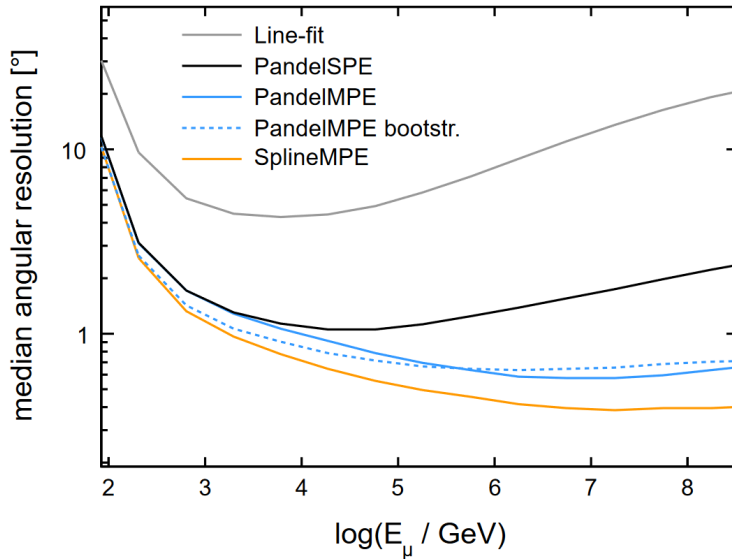
Figure 19: Angular resolution comparison for the given track reconstruction methods over a large range of muon energies.

all four hypotheses, with the minimum of the four being the most probable track classification.

5.4.2 Reconstruction Cuts

This analysis makes explicit use of two reconstructions, track reconstruction SplineMPE and endpoint reconstruction FiniteReco, and to a lesser extent others mentioned as first guess seeds. SplineMPE is used as the main track reconstruction and FinteReco is used as the estimator of the track's endpoint. The position and directional resolution for the muon reconstruction is crucial for this analysis, as the distance between the muon's track and DOM is vital and will be described later. To ensure the reconstruction is sufficiently accurate, a quality cut is imposed on the calculated reduced log-likelihood. The reduced log-likelihood can be found from the calculated

log-likelihood through

$$Rlogl = \frac{\ln \mathcal{L}}{N_{ch} - N_{par}}, \tag{19}$$

where N_{ch} is the number of DOMs present in the fit and N_{par} is the number of parameters in the fit, which for track reconstructions is equal to five (position, charge and time). The reduced log-likelihood provides a general quality variable to cut on, indicating a more probable fit.

A similar quality cut is imposed on FiniteReco to limit through going tracks in the sample. The reason stopping tracks are favourable in this analysis is a muon that stops in the detector must be in the minimum ionizing regime for the majority of the track, except at the end of the muon's life. By removing muon tracks that shoot through the detector, the average energy of the muons is significantly reduced, leaving mainly minimum ionizing muons. In addition to cutting on the likelihood values, a strict spatial cut is imposed on the reconstructed endpoint. This is to limit the amount of false positive endpoints near the edge of the detector where a through going muon can easily be reconstructed as a stopping track.

Table 2 displays the criteria for events to pass selection. Beyond cuts on the reconstructed variables, charge based cuts help reduce the variability in quality of events present in the sample. A cut on the amount of triggered DOMs outside the analysis region is used to reduce the frequency of high energy or potential coincidence events. A cut is also imposed to observe at least five direct photon hits, where the time residual between the unscattered arrival time and the DOM trigger is consistent. It is also checked that an event actually triggered on a DOM in the analysis region.

Analysis Event Cut	Requirement To Pass
Direct photon hits (-15-75 ns residual)	≥ 5
Analysis region hits	> 0
FiniteReco Likelihood ratio of $\frac{\mathcal{L}_{inf}}{\mathcal{L}_{stopping}}$	≥ 10
FiniteReco endpoint Z coordinate	≥ 100 m from bottom of detector
FiniteReco endpoint	≥ 100 m from detector border
Outside analysis region hits	≤ 20
Rlogl of SplineMPE	≤ 10

Table 2: List of event cuts imposed on analysis sample. These conditions are required for the event to make it to the final sample.

5.5 DOM Cuts

After the event cuts have filtered out undesirable events, information from the DOMs can be extracted. At this point, the reconstructed muon track and endpoint have been calculated and DOM cuts correspond to these values shown in table 2. Spatial cuts are then applied to the DOMs shown in table 3, to reduce variability in the photon detection signal. First the DOM must be in the analysis region to contribute any signal. With only the bottom half of the DOM instrumented with the PMT, DOMs that
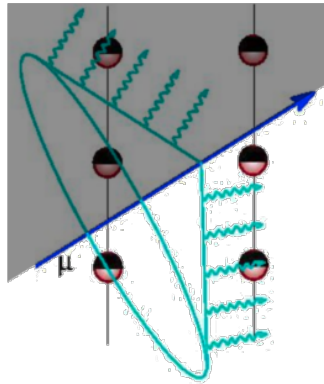
Figure 20: Diagram displaying an example muon track and the resulting DOMs passing cuts in the shaded region.

Analysis DOM Cut	Requirement To Pass
DOM located within analysis region	True
DOM vertical position	$\geq$Closest position on muon track
DOM distance from muon track	$\leq$140 m
DOM distance from endpoint	$\geq$100 m

Table 3: List of DOM cuts for events in final sample. DOMs passing these cuts are considered in the analysis, whether they detected a hit or not.

are located vertically above the tracks closest approach are included as shown in figure 20. DOMs must also be located within at least 140 m of the reconstructed track in an attempt to minimize highly scattered photons and uncorrelated noise triggers. Near the endpoint of the muon, it is no longer a MIP and therefore introduces uncertainty in photon production which is something to be avoided. The reconstruction also has a bias to estimate endpoints beyond the true endpoint, potentially including irrelevant DOMs. To compensate for this, only DOMs located at least 100 m from the track's reconstruction endpoint are considered. It is vitally important to note that DOMs that pass these cuts enter the final analysis, whether they detected charge or not.

6   Analysis Method

The analysis follows a fairly straightforward procedure of comparing the observed charge in data to that in the four simulation sets. A brief overview of how the processing works, then an in depth look at key aspects of the analysis will be given in this chapter. Simulation and data are treated with the exact same method. This analysis pulls from several previous iterations of the measurement of the DOM efficiency, all of which followed a similar approach [68, 40].

6.1   DOM Efficiency Measurement

After the data (or simulation) set has been processed to the final level it can be binned for the final analysis. Only two variables are considered, the amount of charge a particular DOM detected as well as the distance that DOM is from the reconstructed muon track. The charges from DOMs passing all analsys cuts are binned in 20 m track-to-DOM distance bins and averaged. The average charge in each bin for all simulation sets as well as data can be seen in figure 21.

After the average charge has been calculated in each distance bin, the ratio of the Monte Carlo values are taken to data. This gives a representation of the Monte Carlo comparison for various simulated efficiencies. It is expected that the ratio should be fairly horizontal, indicating agreement between the modeled charge response and data at all distances from a source, while deviations indicate potential unknown or unsimulated effects. A relationship can be formed to relate scaled average charge to simulated efficiency. By averaging the data points in the shaded region, justification for this region given in section 6.2.5, for each efficiency, a linear fit can be applied to find the relationship between relative charge observed and simulated DOM efficiency.
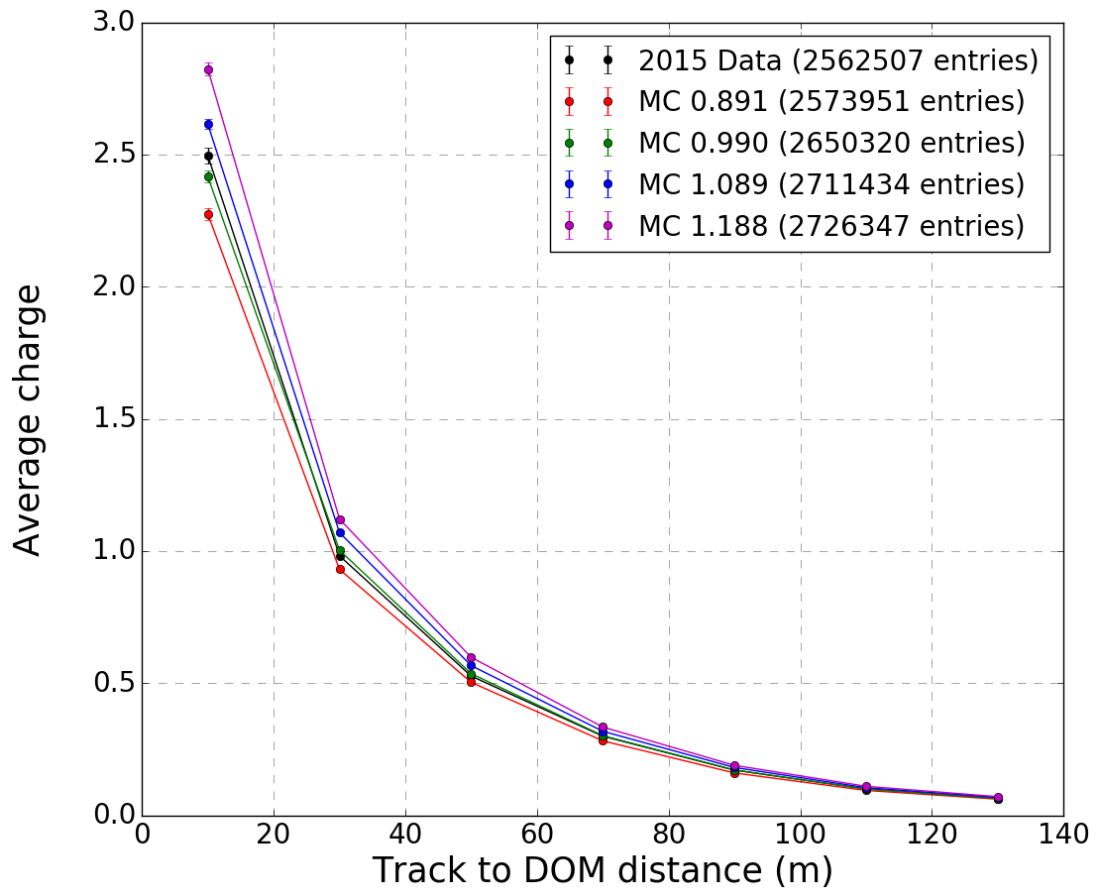
Figure 21: Average charge binned by distance from the muon track for IceCube DOMs. These averages include DOMs which did not detect charge but passed the spatial cuts, resulting in averaged detected charge well below threshold at far distances.

This fit is constructed entirely from the simulated data. Then the relative amount of charge the signal detects intersects this line at the best fit simulated efficiency, and from this result the DOM efficiency factor has been measured.

6.2 Corrections and Consideration

The steps to making the DOM efficiency measurement are quite straightforward once the desired event sample is attained. However, there are several precautions taken to ensure that the sample is as well understood as possible. This is a calibration measurement to describe the charge response of the DOM in situ, and as such all aspects that affect this measurement must be understood. Potential dependencies of this measurement on other detector effects must be analyzed and accounted for in this analysis to ensure that the DOM efficiency factor is truly being measured accurately. Here are outlined several corrections and considerations based on effects observed while making this measurement.

6.2.1 Scaled Charge Gradient

After constructing the relationship for the average scaled charge as a function of the simulated DOM efficiency as seen in figure 36, it was noticed that the gradient of the line did not show a 1:1 ratio. Naively it was expected that an increase of 10% in simulated DOM efficiency would increase the average charge response by exactly 10%. It is important to understand and explain why this effect occurs and if it biases the analysis.

In the simulation the increase of DOM efficiency factor directly increases the number of accepted photons on the DOM's surface, which in turn would increase the photoelectron response in an exact 1:1 proportionality. However we see that the actual

59

increase of about 5.5% average charge for a 10% increase in DOM efficiency.

There exist two main causes for this relationship not to be exactly proportional. The first being the detectors threshold effect when accepting and rejection potential events. For example, a particularly low energy event at nominal efficiency could have just passed under a reconstruction threshold, failing to be reconstructed and thus not entering the sample, but that same event at a higher simulated efficiency was able to be reconstructed successfully due to the addition information. This results in a difference in the energy distributions of the muons passing analysis cuts for each simulated DOM efficiency as seen in figure 22, with lower efficiencies averaging higher energy events. Higher energy event will then produce more observed charge, potentially leading to the observed scaled charge gradient. To test this effect, the full analysis method was run again but only using a subset of events in which all four simulation sets were able to reconstruct adequately. With this sample, of exactly identical events, the gradient showed improvement to the expectation as seen in figure 23, but was still lower than expectation.

The second, smaller effect which impacts this gradient comes from the method in which detector noise is overlaid onto signal in the simulation. The noise generator is modeled after data measurements, and then from this model noise is sampled and added to the pulse series from signal. Importantly, the noise generation in simulation does not scale with DOM efficiency, resulting in a flat amount of noise added across all simulation sets. By adding a flat amount of average charge that is not dependent on the simulated efficiency, the gradient is forced down below the expectation. This effect was then removed by running the detector simulation over the CLSim output with noise generation turned off. Finally, using this sample and the criteria from the previous paragraph the datasets were reprocessed and produced a gradient consistent with expectation in figure 23.

With an adequate explanation of these effects, along with their impact on the analysis, it is safe to proceed with the initial analysis on the sample. The threshold effect would impact data in much the same way it is affecting the simulated threshold. Both simulation and data are processed using the same algorithms, so this threshold effects that comes from processing will be equally present. As for the noise generator, because this is modeled after what is observed in data there is no bias on the measurement. The measurement of the DOM efficiency factor, which is the best simulated efficiency to match data, should use noise modeled after the data it is attempting to match. With both of these effects able to be described, and no discernable effect on the analysis, there is no need to account for them when processing the final levels of data.

6.2.2   Muon Zenith Angle

Initially the analysis has an event cut that only allowed muon tracks from 40° to 70°, where a 0° track represents a muon traveling straight downwards relative to the detector. This cut was initially created to try and reinforce the notion that tracks passing this requirement would have their produced Cherenkov photons incident on the sensitive half of the DOM. This is a valid consideration when describing a two dimensional situation. In the extreme example a track coming in at 40° will have a portion of photons emitted horizontally, or slightly upwards as the Cherenkov angle in ice is $\sim$42°, when considering only a two dimensional case. But when considering three dimensions the majority of the photons produced are not incident on the DOM's sensitive surface. The true direct photon arrival angles incident on the DOM's surface can be seen in figure 24. As the intention of this cut was to reduce the number of photons incident on the insensitive half of the DOM, something that is clear to happen still, the cut was removed in favour of increased statistics as can be seen in figure 25.
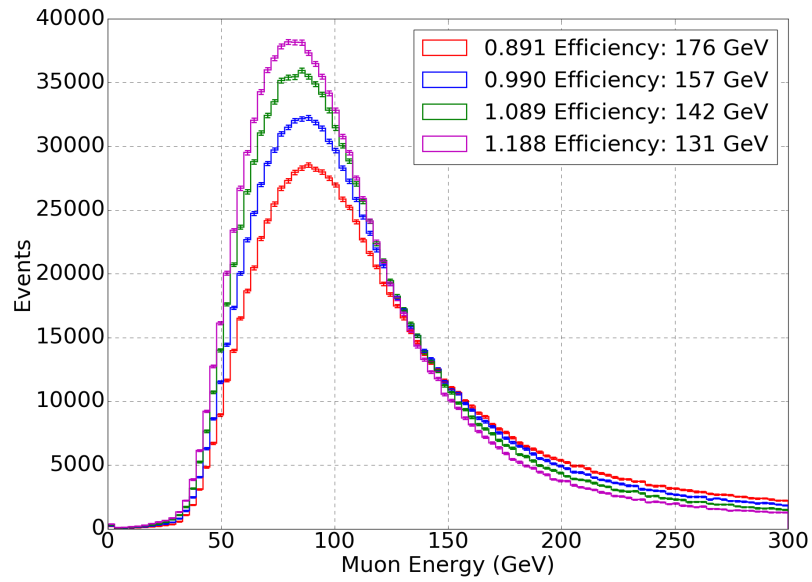
Figure 22: The energy spectrum of muons from each simulation set. The energy is shown in the legend corresponding to the average energy at which the muon intersects the analysis region to verify minimum ionizating muons in the analysis region. For reference, the critical energy for muons in water is roughly 1 TeV.
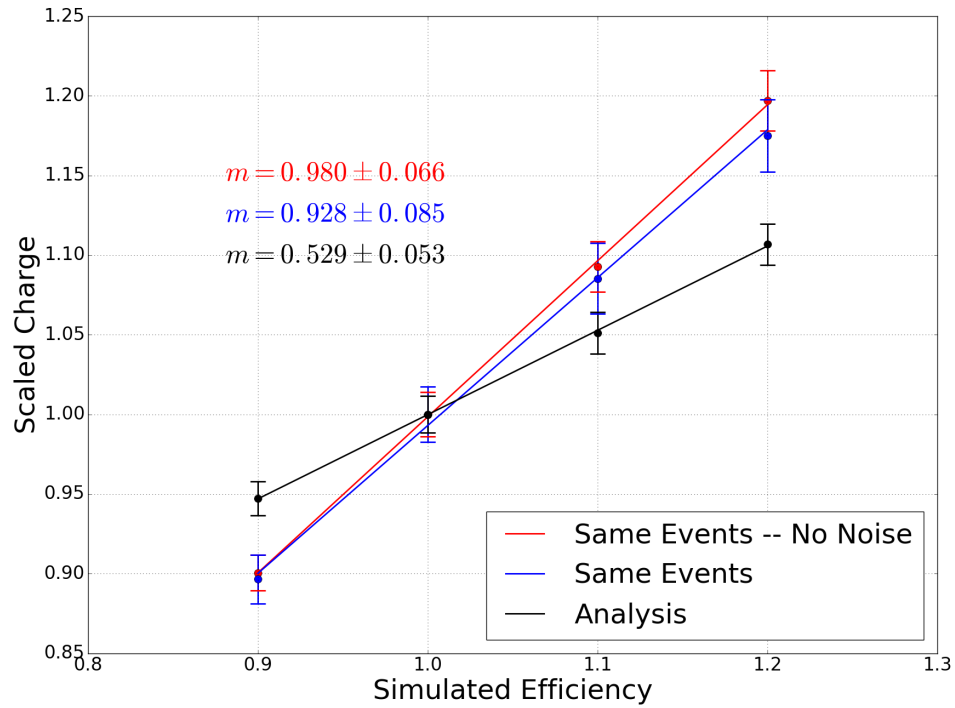
Figure 23: The average scaled charge relationship is shown here. In black is at final analysis levels, whereas the blue represents the analysis level cuts but using mutual events in all simulation sets. The red represents if noise is excluded from the blue line.
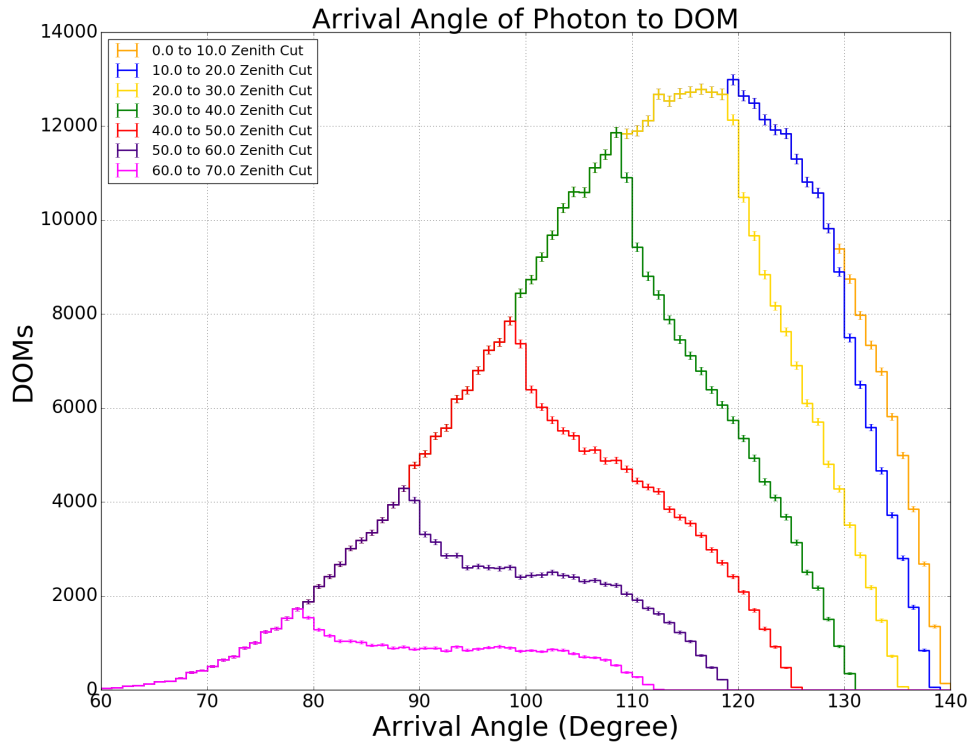
Figure 24: The arrival angle distribution of the muon tracks to DOMs for nominal simulated efficiency. Angles greater than 90° are incident on the sensitive surface of the DOM. The stacked histogram is sliced in muon zenith angle bins, showing the distribution of arrival angles for a particular zenith angle cut.

6.2.3 Muon Bundles

From the cosmic ray flux models used in the dCORSIKA simulation as well as the hardonic interaction model SIBYLL 2.3, a calculated spectrum and multiplicity of muons is generated. The multiplicity of muons in an air shower is an indicator of the primary cosmic ray type and energy, and the interaction models in simulation use this information. There has been a noticeable mismodeling of the muon multiplicity distribution, seeing nearly an order of magnitude increase in the flux of higher muon

multiplicity events compared to real signal [69]. In IceCube these events can be characterized by containing several muons with a small opening angle spread, known as muon bundles. IceCube does not currently have a robust method for reconstruction multiple simultaneous muons. Having a potential mismodeling of the flux of such events is concerning and as such there is an attempt to remove such events from the final analysis sample. Historically in this analysis, the reconstructed muon zenith cut outlined in section 6.2.2, was thought to have solved this problem.

A muon bundle could be detected and passed into the final analysis sample, depositing an inconsistent amount of energy when compared to single muon tracks, something that should be avoided. These bundles are extremely hard to discriminate at these energy levels, as any single muon event produces a small amount of light in the detector, on the order of five pulses in the analysis region. The idea behind the zenith angle cut is that the amount of overburden the muons have to traverse increases with reconstructed zenith angle, and at higher overburden levels muon bundles would be more likely to range out before reaching the detector.

The muon multiplicity contaimination can be found in the simulations true information, and as can be seen in figure 25, the contamination of bundles in the simulation sample can be decreased modestly by cutting on the reconstructed muon zenith angle. Initially this cut was at 40°, cutting away the straight down going tracks in the sample, but this only decreased the bundle contamination by approximately 1%. Meanwhile this cut reduces the raw statistical power of the analysis sample by 66%. This sacrifice of statistics for the increased purity was not deemed as a gain for the analysis.

In an attempt to replace this intended cut to targeted at bundles, it was thought that the total amount of deposited charge in an event could give a handle on discriminating the bundle events from the sample. Shown in figure 26, the summed charge from all DOMs participating in the event is shown. Naively the amount of charge in a
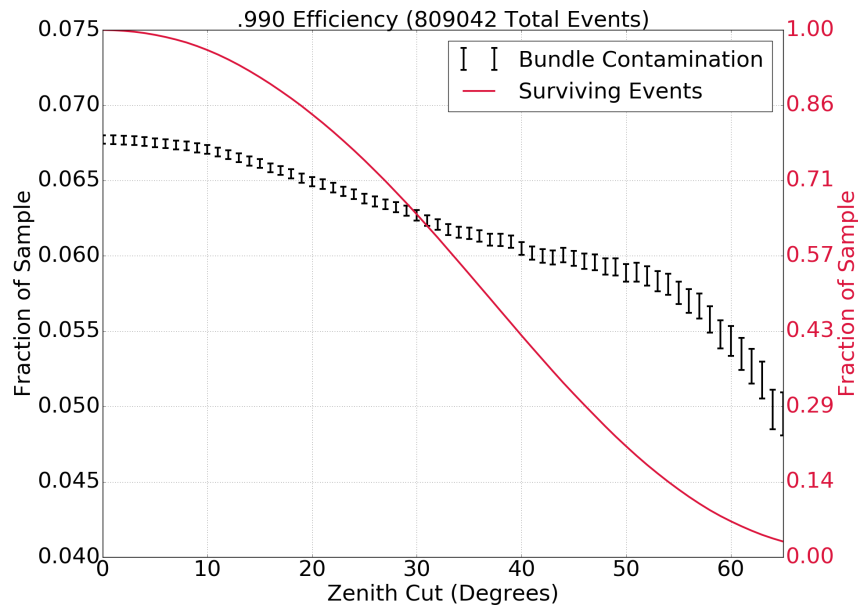
Figure 25: The effect of the reconstructed zenith angle cut on the sample is shown, with the angle cut increasing in stringency at higher angles. Bundle contamination events are characterized as having two or more muons cross the analysis region in a single event window. The fraction of bundle events in the sample can be read off the left axis corresponding the the black data points, while the surviving amount of the entire sample can be read off the right axis corresponding to the red solid line.
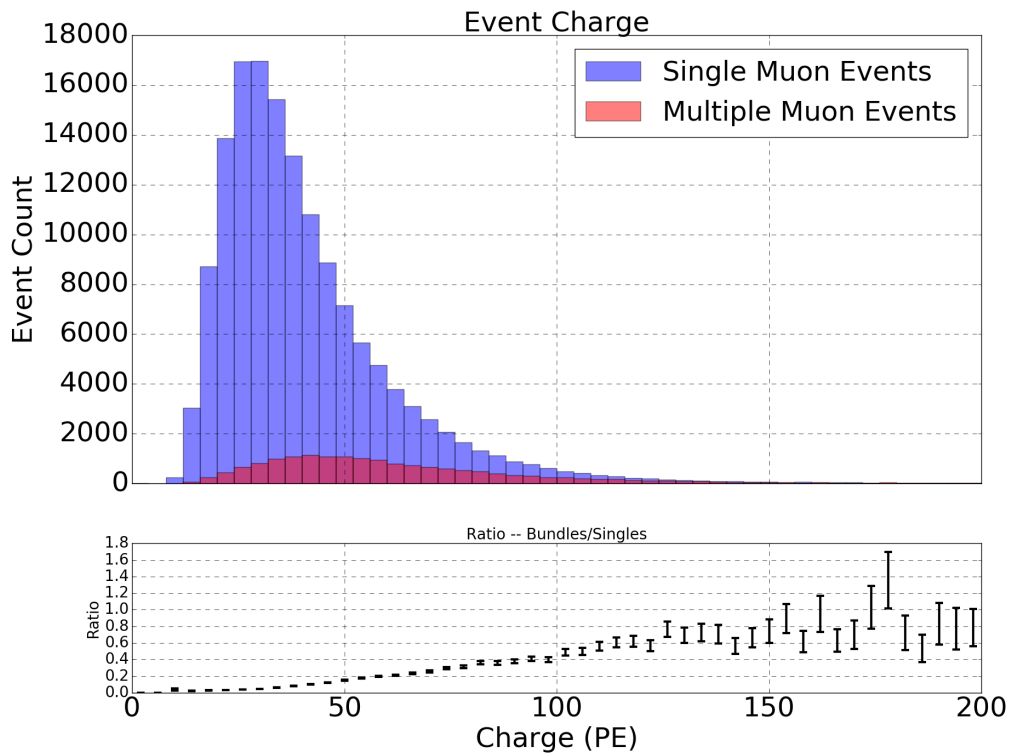
Figure 26: Total event charge for nominal DOM efficiency, events are split between events containing a single muon and events with multiple muons passing through the analysis region. Below shows the ratio of the counts in bins, showing at higher energies bundle events are more likely.

bundle event should roughly be double of that in a single event, but as can be seen the distributions are not very well separated. Several additional variables, none of which showed any better separation, were also investigated, but no straight cut on any variable proved to be useful. With no clear solution, no cut was imposed to target the bundles but rather an error enters the analysis associated with the uncertainty in the simulation regarding bundle production.

To account for the uncertainty associated with the production and enhanced charged contribution due to bundles, a simple calculation is done. The charge contribution of bundles, q_b, is calculated through,

$$q_b = \bar{q} \, \frac{\bar{q}_{bundle}}{\bar{q}_{single}} \frac{N_{bundle}}{N_{total}}, \tag{20}$$

where the ratio of $\bar{q}_{bundle}$ to $\bar{q}_{single}$ represents the ratio in charge deposited in bundle events and non-bundle events, and $\frac{N_{bundle}}{N_{total}}$ represents the amount of the sample that are bundle events, and $\bar{q}$ is the average charge detected over all the DOMs. In addition there is error in the hadronic model which can cause mismodeling of muon multiplicity, but this is a minor effect on the overall contribution. The error on q_b then represents the uncertainty in averaged charge due to the muon bundles. Through basic error propagation, this uncertainty comes out to be 0.00077 photoelectrons, this can be compared to the measured values in figure 21.

6.2.4 Reconstruction Performance

A short overview of the resolution of the reconstruction algorithms will be looked at. For the analysis, the only parameter that is influenced by the reconstruction of the event is the track-to-DOM distance, whereas the charge is a result from the de-
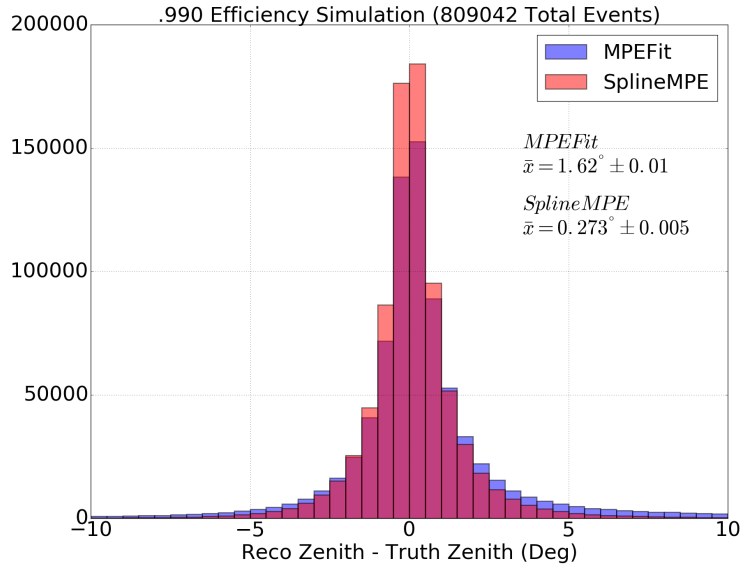
Figure 27: The difference (subtraction) between the reconstructed track zenith angle and the true muon zenith angle for nominal DOM efficiency simulation. Two reconstructions are displayed to show the improvement made in angular resolution when switching from MPEFit to SplineMPE.

tector's response. Historically the sample used MPEFit, as discussed in Section 5.4.1, but this proved to have an innate bias as shown in figure 27. Cumulative angular resolution of the fits can be seen in figure 28. The consequence of having the sensitive side of the DOM facing downwards manifests itself in a slight bias in the reconstruction algorithms which favour reconstructing tracks to be slightly more horizontal than the true track. As the muon passes DOMs, they are more likely to detect charge if the DOM is vertically above from the Cherenkov angle relative to the muon track, resulting in a likelihood fit favouring tracks below the DOMs. As can be seen in figure 27, MPEFit has a 1.62° bias in this direction, whereas the SplineMPE reconstruction minimizes this effect, but does not completely remove it. This effect leads to an average uncertainty that will be discussed in the following section 6.2.5.

69
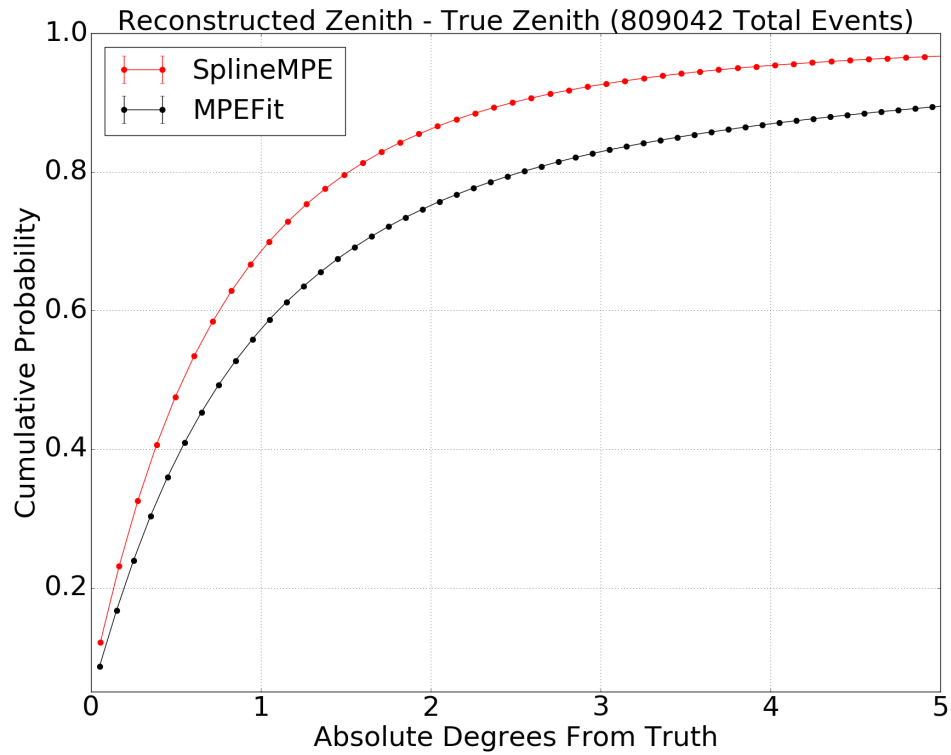
Figure 28: The cumulative probability of the reconstruction algorithm to produce a track within an angle relative to the true track for nominal DOM efficiency. Comparison is shown between MPEFit and SplineMPE.

The endpoint reconstruction for the muon track, FiniteReco, also has short comings in terms of performance that must be mitigated. As was discussed in Section 5.4.1, the likelihood function relies on the probability of DOMs near the predicted endpoint detecting charge while DOMs further along the track observe nothing. It is not uncommon for the muon track to not produce light near the true endpoint, giving the endpoint reconstruction difficulties. This creates the case where endpoints are reconstructed with confidence early on in the track while the true endpoint extends up to hundreds of meters further along the track. Cutting on the likelihood ratio, the difference of the stopping track hypothesis and infinite track hypothesis log-likelihood values, allows for quality control of the reconstruction in an attempt to mitigate this effect. The effects of this cut can be seen in figure 29. From this information it was decided that the cut value would be set at 10, which reduced the average separation between the reconstructed and true endpoint to ∼50 m while keeping 50% of the sample.

6.2.5 Reconstruction Bias and Error

Having the track reconstruction bias previously mentioned, the tracks are being reconstructed to be slightly more horizontal than their true information. This creates a bias in the track-to-DOM distances due to how the DOMs are accepted into the final level analysis. The DOMs must be vertically above the reconstructed track, and if this track has been reconstructed to have a larger zenith angle, this in turn pulls the track further from the DOMs. This biases the track-to-DOM distances to be slightly higher on average than the truth. This effect can be seen in figure 30, wherein the true track-to-DOM distances in a single 20 m reconstructed track-to-DOM distance bin can stretch extremely far from the expected distance.

An investigation was also conducted on the potential bias of the track recon-

71
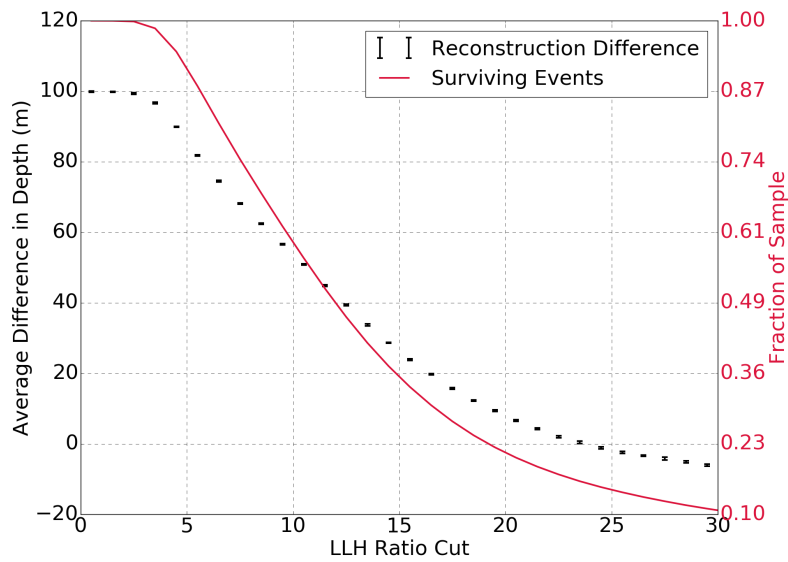
Figure 29: The average difference between the depth of the reconstructed muon endpoint and the true muon endpoint shown in the data points for different cut values of the likelihood ratio. The line shows the fraction of the sample surviving the cut.
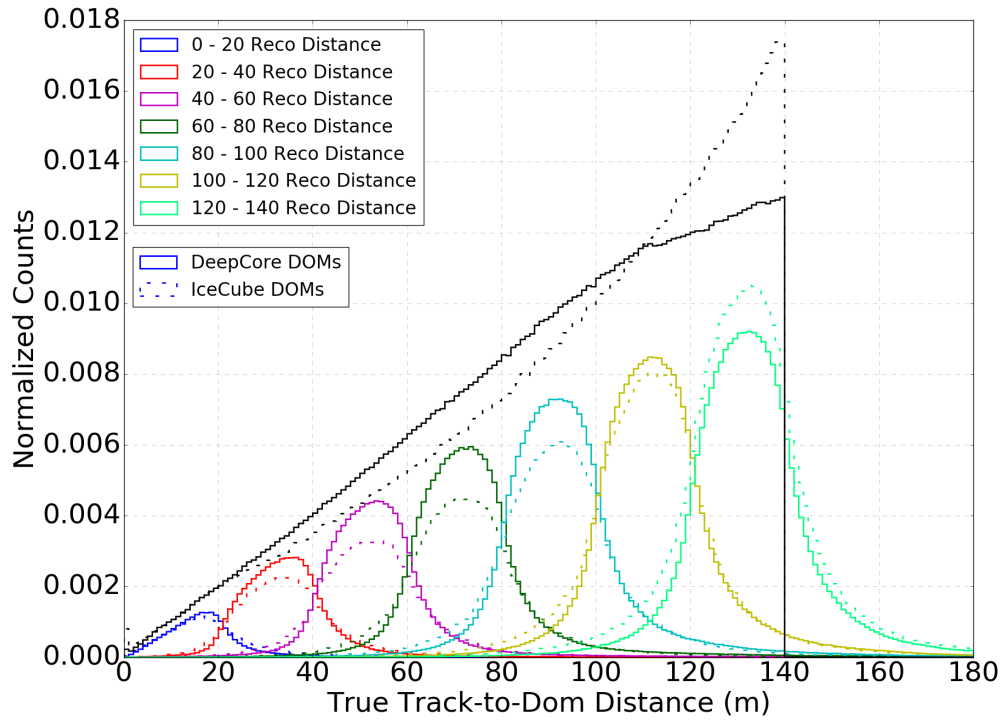
Figure 30: The analysis bins the reconstructed distance from muon track to DOM in 20 m distance bins. The distribution of true track-to-DOM distances are shown for each of these bins, treating IceCube (faded lines) and DeepCore (solid lines) DOMs separately. The total distribution for reconstructed track-to-DOM distances can be seen in the black distribution cut at 140 m.

struction, where particularly bright DOMs would heavily pull the reconstructed track. To test if this is the case, a set of analysis events were reconstructed again after removing a random fifth of the DOMs in the pulse series. This was replicated five times, removing a unique set of pulses from the series each time to span the entire series. For each set of fits on the subset of pulses, DOMs not participating in the fitting procedure are then used to sample reconstructed track-to-DOM distances. After preforming this procedure five times the track-to-DOM distances were compared to those from the fit containing all DOMs. There is no bias, although there is a spread due to failed reconstructions from lack of the full information The difference due to these reconstructions can be seen in figure 31.

The spread distributions seen in figure 30 for each reconstructed distance bin translate into a bias in the average charge observed by a DOM. To get a handle on what kind of uncertainty is introduced here, the average charge per 20m distance bin is calculated for DOMs which were reconstructed in that bin and for DOMs that should have truly been in the bin. The ratio of these averaged charged values can be seen in figure 32. A noticeable feature is the average charge is underestimated in every bin, this is a result of a proportionally larger fraction of track-to-DOM distances that extend much further than the designated distance bin. This translates into DOMs that are futher away from the track and therefore less likely to observe charge being placed in close distance bins and thus reduce the average charge in the bin. As can be seen, the 40 m-100 m distance bins replicate the true charge information the best and therefore these bins are used in the actual analysis. From these three bins the absolute deviation of the average charge can be calculated from the truth, -0.0064 ± 0.0016 photoelectrons, which is the dominant source of systematical uncertainty in this analysis. The uncertainty on this average charge deviation enters as the error on the average charge in figure 21.

74
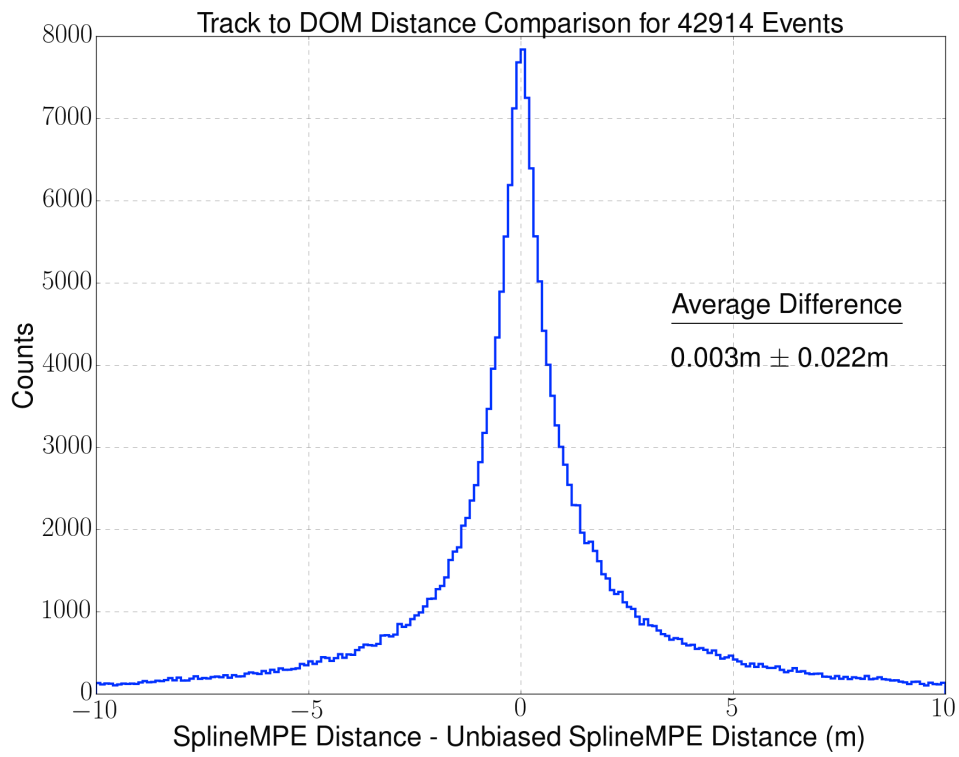
Figure 31: The difference in track-to-DOM distances from the full pulse series fit and the five partial, unbiased series fits.
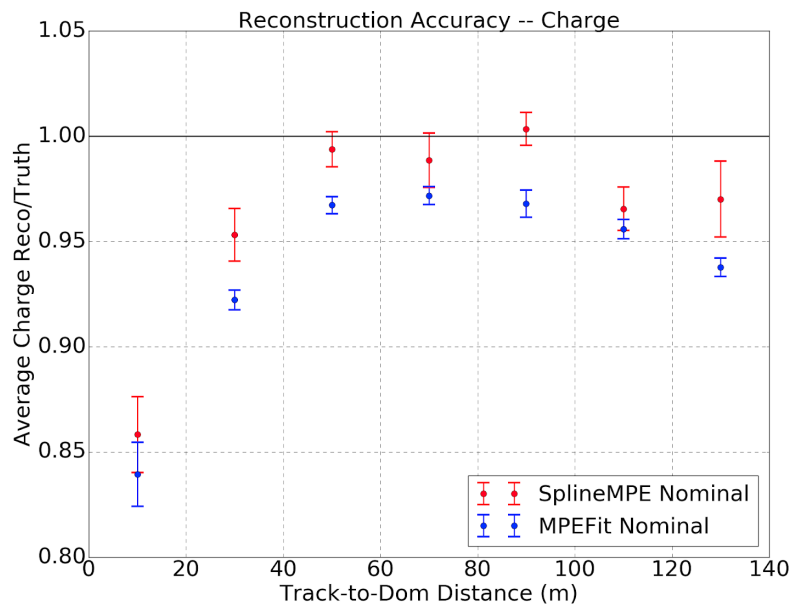
Figure 32: Ratio of averaged charge measured in the reconstructed bin to true information from figure 30. A comparison is shown between SplineMPE and MPEFit to demonstrate the improvement of the reconstruction.

6.2.6 Dust Layer Contamination

When comparing the Monte Carlo to data, a systematic bias was found in the amount of charge detected at the top levels of the analysis region. To understand this discrepency, the amount of charge was plotted as a function of track-to-DOM distance in simulation, much like it is for the final analysis processing, and compared to the same distribution in data. The ratio of simulation to data was taken in each charge bin. This was tested over varying depths in the analysis region to look for variation, indicating a mismodeling effect.

This comparison indicates that the simulation is not correctly taking into account the boundary between the dust layer and the clear ice. If the dust layer extends metres lower in reality than the simulation model, then the ice is being treated as being much clearer and less absorptive. This results in the scattering and absorption lengths being longer in simulation in this mismodeled region. Based on the findings in figure 33, this theory is consistent with the contaminated region disagreeing more track-to-DOM distances increase allowing for variations in the ice properties to affect the sample. The photons in data are being scattered and thus absorbed more often, resulting in an average charge per bin lower than that seen in simulation.

While this discrepancy requires a bit more investigation to be completely understood, the solution put forth here is to not include these depth levels in the analysis. A separate analysis could look further into this mismodeling, but the goal of this analysis is to understand the in situ DOM performance and attempt to decouple it from incorrectly simulated effects. For a complete solution, this would indicate that a re-modeling of the dust layer in simulation would need to be done, essentially extending the effects of the dust vertically down.
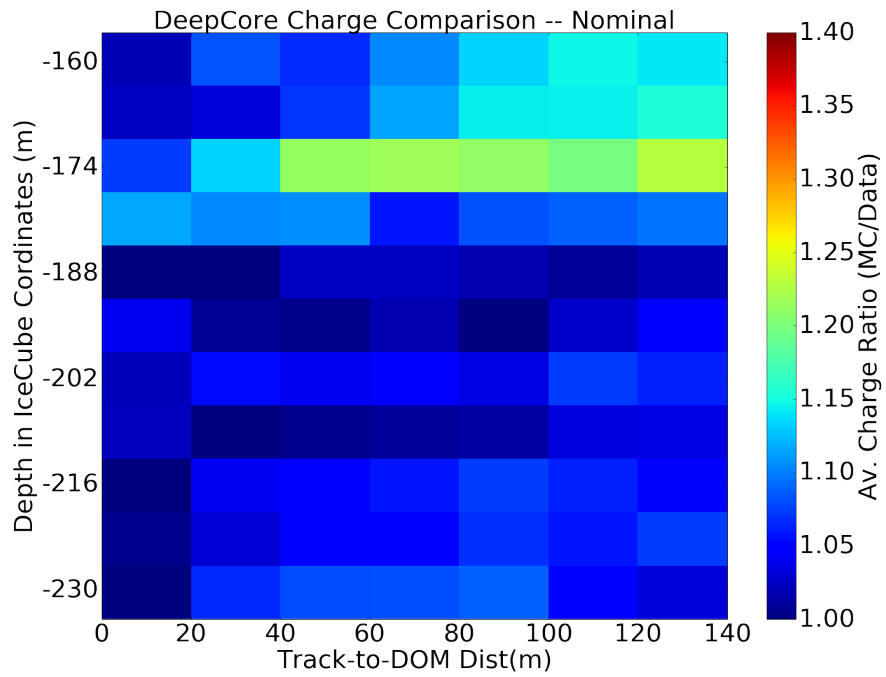
Figure 33: The average charge per bin ratio between Monte Carlo and data. Each bin depth represents a single DOM layer in Deepcore, vertical spacing of 7 m. The discrepancy can be see in the top ~15 m of the analysis region.

6.3 Statistical Errors

The statistical errors of the sample in this analysis are mainly treated through bootstrapping [70]. The distributions being dealt with are mainly heavily one tailed, non-negative distributions centered at near zero values, in which a simple standard error calculation is not entirely valid. An example of this can be seen in the muon energy distribution in figure 22, where the large tail leads to unreliable standard error calculations. Bootstrapping is an extremely simple and effecticve method to estimate confidence intervals at the price of being computationally expensive. This method calculates an estimate for an expectation value $\bar{x}$ from a distribution of N samples. A random amount from the distribution is drawn, ranging from 1 to N samples, with replacement of the drawn sample before the next is chosen. From this subset of the population, the mean is calculated. This process is done several times and the spread of the means calculated follows a normal distribution. From this the estimator for the true mean and its standard error can be directly calculated. Bootstrapping relies on the independence of each sample as well as the randomness of the resampling, which is satisfied in this analysis. The disadvantage comes in the form of computational speed, for distributions containing a large number of samples this approach can be extremely slow.

For calculating the average charge in each distance bin, as is done in figure 21, the distributions have too many events to effectively utilize the bootstrapping method. This is also complicated by the fact that the events in the sample are weighted according to a flux model, as is discussed in Section 4.5. The charge in a particular event will also carry the weight. The averaged weighted charge calculated in a particular distance bin is given by,

$$\bar{q} = \frac{\sum q_i w_i}{\sum w_i} = \frac{A}{B}, \tag{21}$$

the statistical error on $\bar{q}$ would be calculated through simple error propagation,

$$\sigma_{\bar{q}} = \bar{q} \sqrt{\left(\frac{\sigma_A}{A}\right)^2 + \left(\frac{\sigma_B}{B}\right)^2 - 2\frac{\sigma_{AB}}{AB}}. \tag{22}$$

The third term refers to the correlation between σ_A and σ_B, known as the covariance of the two variables. The value of σ_A^2 and σ_B^2 can be written as,

$$\sigma_A^2 = \sum \left(q_i w_i\right)^2 \tag{23}$$

$$\sigma_B^2 = \sum \left(w_i\right)^2, \tag{24}$$

as is discussed with weighted variables in ref. [71]. Also suggested for the covariance term is,

$$\sigma_{AB} = \text{cov}[A, B] = \sum w_i(q_i w_i), \tag{25}$$

which leaves the statistical uncertainty on the average weighted charge to be,

$$\sigma_{\bar{q}} = \bar{q} \sqrt{\frac{\sum \left(q_i w_i\right)^2}{(\sum q_i w_i)^2} + \frac{\sum \left(w_i\right)^2}{(\sum w_i)^2} - 2\frac{\sum q_i w_i^2}{(\sum q_i w_i)(\sum w_i)}}. \tag{26}$$

6.4 DOM Systematics

Additional systematic effects must be investigated as they also contribute to the overall uncertainty on the measured DOM efficiency. For example the PMT's noise rate can be mistaken for signal and must be accounted for. The noise has been measured

and is shown in figure 34, and is modeled in simulation based on the measured values. This means the raw amount of noise in the signal and simulation should be similar, but the uncertainty regarding the noise produced will shift these values. Taking the time window of events in the analysis, 1 μs, and the average noise a DOM experiences, the average charge due to noise can be calculated. For this analysis, the average charge from noise comes out to $(4.87 \pm 0.04) \times 10^{-4}$ photoelectrons per DOM per event. In addition to noise hits, the PMTs used also suffers from siginicant afterpulsing. Afterpulsing occurs when the photoelectron ionizes a gas molecule in the PMT which after some time de-excites releasing radiation that can cause an avalanche in the dynode chain. These afterpulses are prominent up to several microseconds after the initial pulse is detected. Rough measurements have shown that for a single photoelectrons, the amount of afterpulses is 0.00018 times the photoelectron count detected [72]. Using this information it can be calculated that the rough contribution of afterpulsing to the most active distance bin is only $9\mathrm{x}10^{-5}$ photoelectrons per DOM per event. Both these effects are quite negligible as the average charge is orders of magnitude higher.

6.5   Results

From all these corrections and considerations, the final result for the IceCube DOM efficiency factor can be measured according the the method describe in secton 6.1. The average charge observed by DOMs in each simulation dataset is scaled to the amount observed in the nominal efficiency simulation. A linear fit is then preformed on the relative amount of charge and the DOM efficiency the simulation was run at. After scaling the amount of charge seen in the signal dataset, the DOM efficiency that best describes signal can be determined. The measured DOM efficiency is 0.984 ± 0.006 (statistical) ± 0.022 (systematic) from figure 36. This is an indication
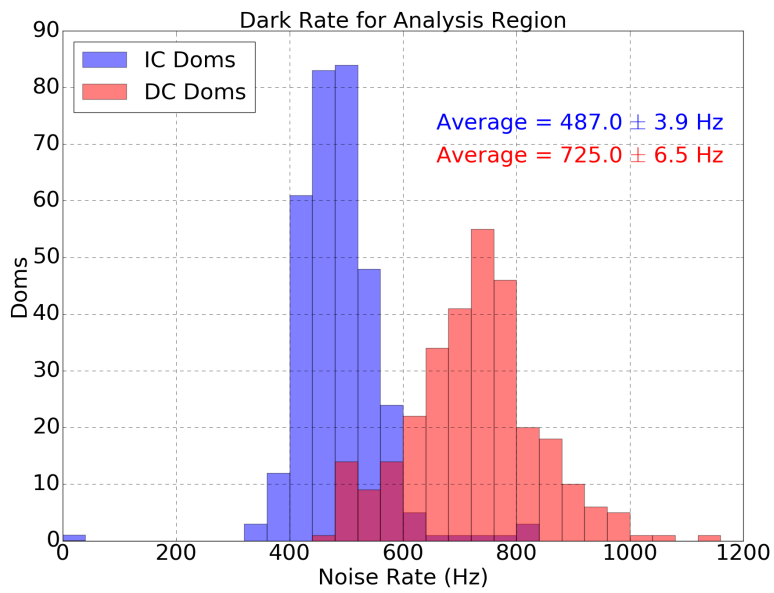
Figure 34: Shown is the average dark noise rate of the DOMs in the analysis region. High quantum efficiency DOMs suffer from a higher noise rate.
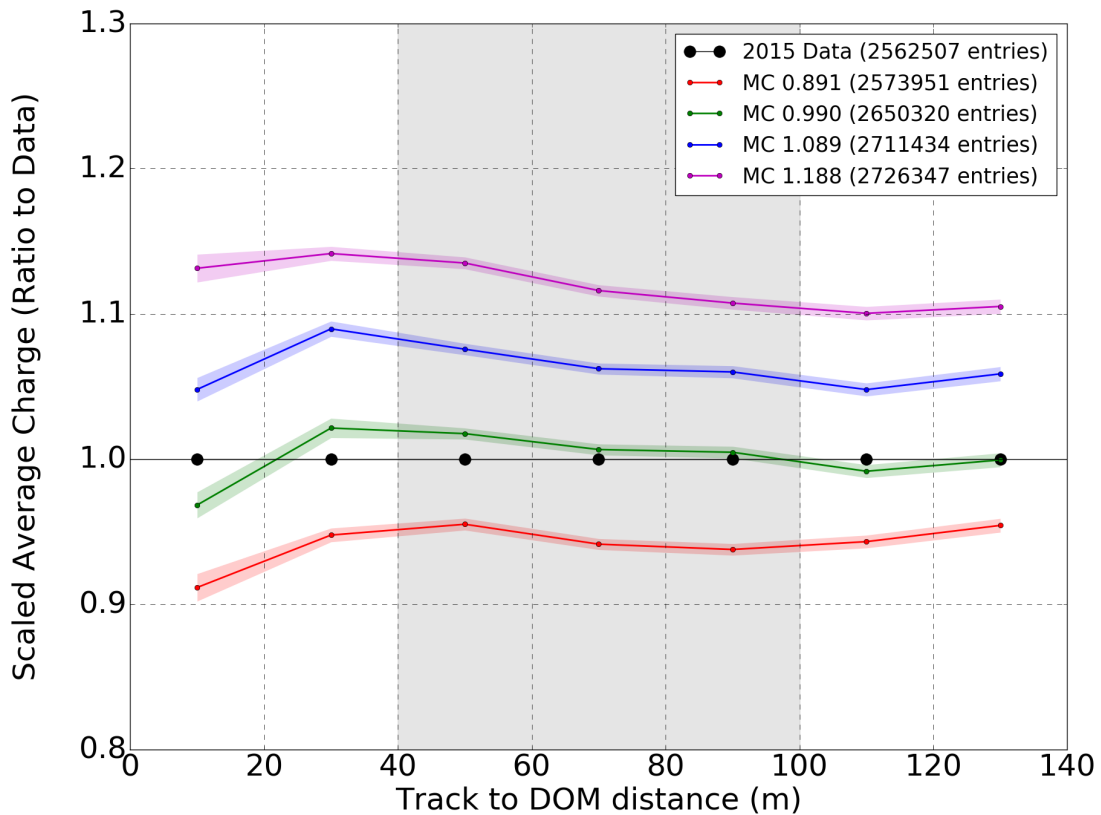
Figure 35: The scaled (to data value) average charge in each distance bin from figure 21. The shaded region refers to data contributing to final result.

that the simulation is detecting slightly too much charge and needs to be scaled down by $\sim 2\%$ to match data. The uncertainty on this result is limited by the systematics included in this analysis. The DOM efficiency factor currently in use for all analyses is at 0.99 ± 0.10 which show agreement with the results found in this study.

6.5.1 DeepCore Results

This analysis is done in a general way and was focused primarily on measuring the DOM efficiency of the IceCube DOMs. DeepCore is instrumented with the higher
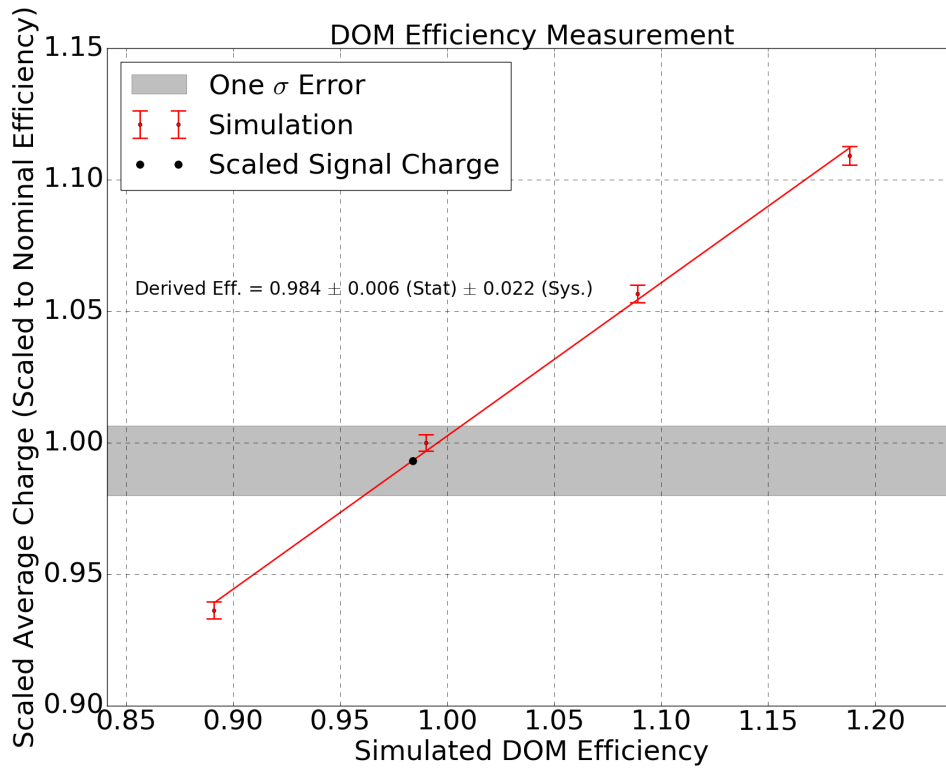
Figure 36: After averaging over charge detected in DOMs in the shaded region of figure 35, and scaling the average charge for each simulation set to the nominal value, the relationship between scaled average charge and simulated DOM efficiency. The average charge oberserved in data for this region is then scaled by the same nominal value and the best fit DOM efficiency parameter is found. A one sigma error band on the best fit DOM efficiency factor is shown.

quantum efficiency (HQE) DOMs, which are documented having a similar design to the nominal DOMs but just differing quantum efficiency. Initially it was thought that the measured DOM efficiency should be sufficient in describing the correction factor for both types of DOMs. However this does not appear to be the case as seen in figure 37 where the measured DeepCore DOM efficiency factor is 0.9231 ± 0.004 (statistical) ± 0.033 (systematic), again dominated by systematics. This is concerning as the simulation is built to only parameterize the DOM efficiency of the entire detector through one variable, indicating that if things are functioning as expected the DOM efficiency measurement should agree between the HQE and nominal DOMs.

Understanding why the HQE measurement is not in agreement to the normal QE measurement is still an open question but some investigation has been done. At the simulation level, the DOM efficiency factor for the HQE DOMs is simply multiplied by 1.35, the rough increase in quantum efficiency over the nominal DOMs as measured *in situ* [52]. This should in turn result in a rough increase of about 35% more photoelectrons in the HQE DOMs. The resulting measurement does not agree with this, potentially indicating that the in situ photon acceptance of the HQE DOMs is not properly understood. This then creates a discrepancy between the simulation and data reponses of DeepCore that can not be readily explained. As seen in figure 38, the ratio of charge observed in the HQE DOMs compared to the nominal DOMs is not consistent between simulation and data. This indicates an unknown mismatch potentially casting doubt on the charge response in DeepCore. Based on findings in this analysis, a likely cause for this is a mismodeling of the HQE DOMs in simulation. The DOMs in simulation are modeled as having too high of a photon acceptance compared to reality. Expanding off of this theory, the simulation would more easily be able to reconstruct events of a lower energy, thus having a lower energy threshold than reality. This is extremely hard to test as low energy muon reconstructions do a poor job at resolving

85
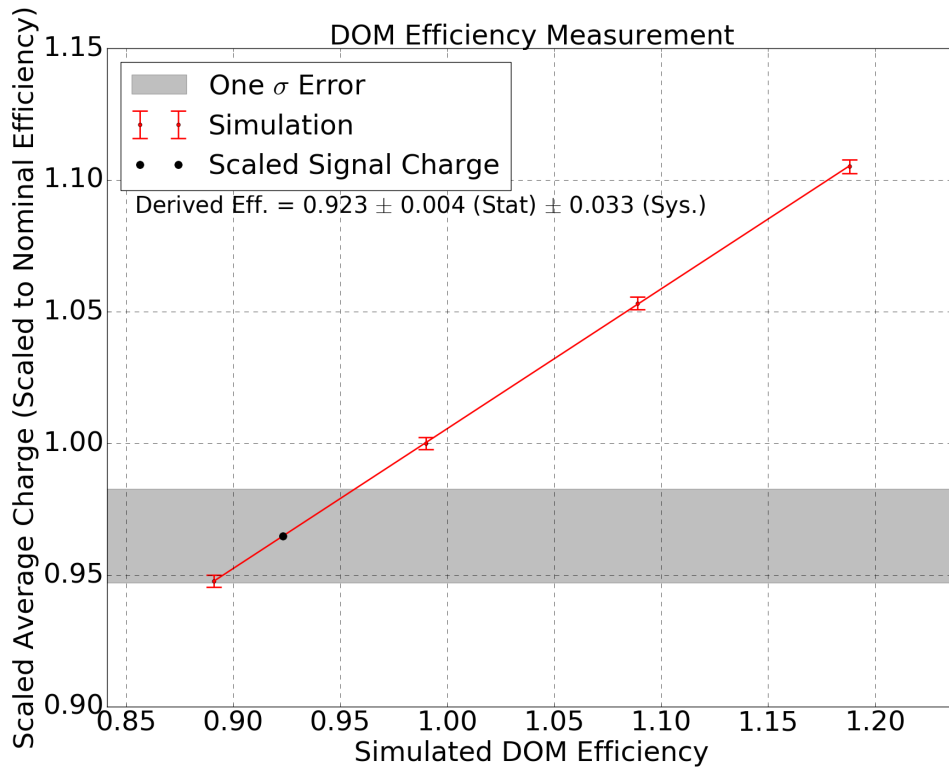
Figure 37: Similar to figure 36 except for the high quantum efficiency DOMs. The measured efficiency is noticeably lower than the result for the nominal DOM.
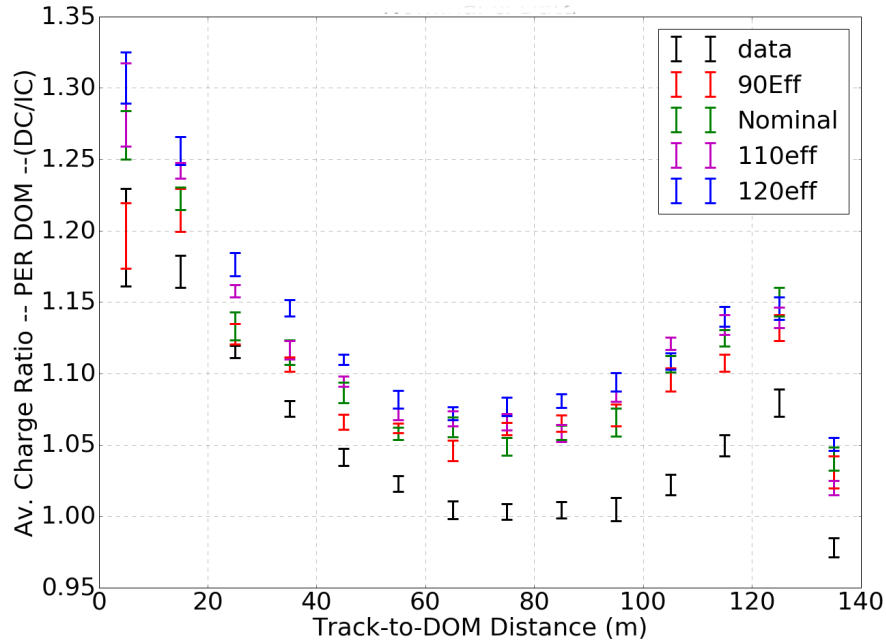
Figure 38: The average charge for the DeepCore (HQE) and IceCube (nominal) DOMs is calculated and a ratio is taken on a per bin basis. Noteably the simulated sets all follow a similar ratio, whereas they disagree with the data.

the muon's energy. Instead, the total charge in each event is then used as a proxy for energy. For each simulation set, as well as data, the total event charge can be seen in figure 39. Just by eye it is noticeable that the distribution representing reality is shifted to contain slightly higher charged, and by proxy higher energy, events than the simulation sets. This does not prove a mismodeling of the HQE DOMs, but gives evidence further investigation of the simulation is recommended.

6.5.2 Proposed Simulation Updates

Recent developments in low level simulation production has motivated the need for a resimulation of several datasets in IceCube. The underlying template that describes the single photonelectron peak, the response from detecting a single pho-

87
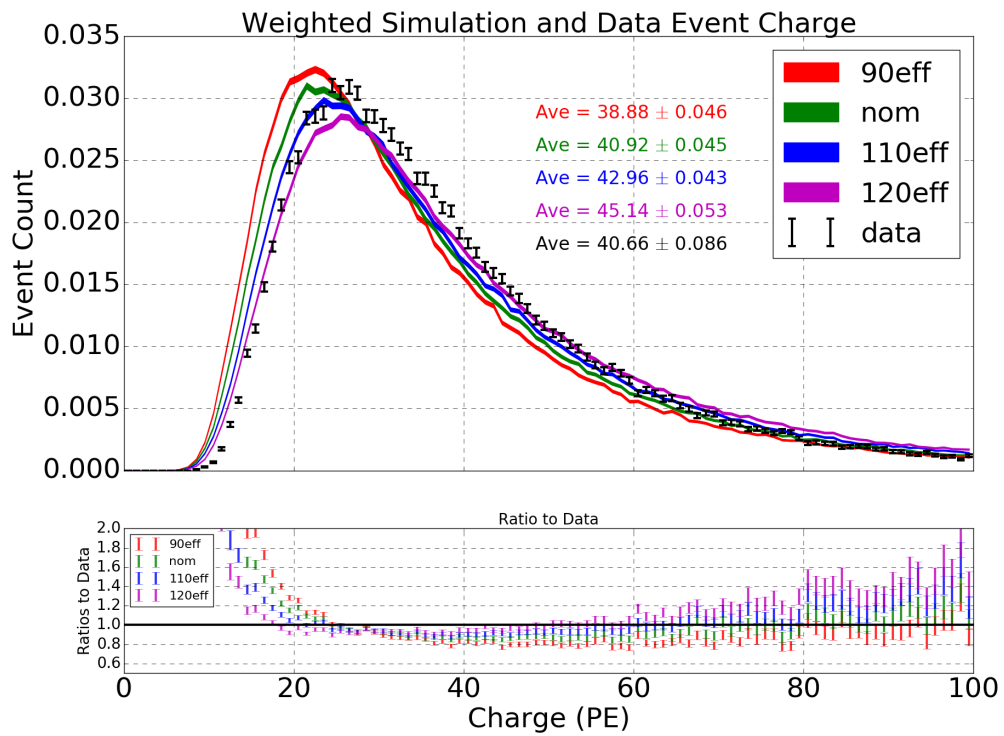
Figure 39: The total event charge can be seen for each simulated efficiency as well as data. Total event charge is the best proxy available for muon energy.

ton, was remodeled to more accurately describe the measured charge distribution. This shifted the distribution by approximately 30% which is extremely important for this analysis, where single photoelectrons make up the majority of the signal. This shift in the template is combined into a scaling factor in simulation, not related to the DOM efficiency factor, so ideally the DOM efficiency measurement should not shift wildly from this change. Unfortunately, there is no way around correcting this issue without a full resimulation beginning at photon propagation in CLSim. Unfortunately, a resimulation of statistically equivilant sets would take $\sim$4 months to complete based on rough estimations, which is beyond the scope of this work.

In addition to correcting for the SPE template update, this provides an opportunity to investigate other aspects of this analysis. As discussed in the previous section, the HQE DOMs should be adapted in simulation to accomodate a unique DOM efficiency factor, seperate from the IceCube DOM efficiency factor, to investigate the disagreement between the measured factors in this work. Another unknown dependency in this analysis is how correlated the DOM efficiency measurement is to the ice model used. If resimulation is done, systematic sets should also be produced to understand the effects of varying the absorption and scattering lengths of this ice. This opens up a wide variety of possible dependencies that have been otherwise neglected in this analysis.

7   Conclusion

The IceCube detector utilizes PMTs to observe the Cherenkov radiation produced by highly energetic electrically charged particles in the deep Antarctic ice. The PMTs are encased in a pressure sealed housing, the digital optical modules (DOMs).

The PMT has been characterized in the lab, but no absolute calibration has been done for the in situ instrumentation. This analysis was conducted to measure the effective difference in the performance of the DOMs ability to detect charge when compared to the models used in simulation. These models are constructed to replicate detector operation and are used to simulate the detectors response to potential events. The DOM efficiency factor in these models adjusts the raw number of photons accepted on the surface of the DOM. By tuning this parameter, the average charge reponse of simulation can be brought in line to better match what is observed in IceCube data. To do this a sample of atmospheric down-going muons is selected, the main background for IceCube. The sample is filtered to be dominantly comprised of minimum ionizing muons, as they have extremely well modeled energy loss processes. By comparing the amount of charge seen in these events from the IceCube detector to four simulation sets of similar events at differing DOM efficiency parameters, the true DOM efficiency factor that best describes the data can be determined.

From this analysis, the measure DOM efficiency factor for IceCube (regular quantum efficiency) DOMs was found to be 0.984 ± 0.023 and for DeepCore (higher quantum efficiency) DOMs was found to be 0.923 ± 0.033. The currently used single simulation value for this parameter is 0.99 ± 0.10. The measurement for IceCube is consistent with this current value and was measured with higher precision. Potential reasons for the discrepancy observed between the IceCube and DeepCore factors has been discussed, but the proposed solution is to parameterize different DOM types separately. As IceCube moves forward, this analysis can be generalized and applied to various types of new DOM instrumentation as a tool for calibration.

References

[1] M. Tanabashi et al. "Review of Particle Physics". In: *Phys. Rev. D* 98 (3 Aug. 2018), p. 030001. DOI: 10.1103/PhysRevD.98.030001. URL: https://link.aps.org/doi/10.1103/PhysRevD.98.030001.

[2] Laurie M. Brown. "The idea of the neutrino". In: *Physics Today* 31.9 (1978), pp. 23–28. DOI: 10.1063/1.2995181.

[3] *Rapports du Septième Conseil de Physique Solvay*. Gauthier-Villars, Paris: Springer, 1933, p. 324.

[4] James Chadwick. "Bakerian lecture.―The neutron". In: *Proceedings of the Royal Society of London. Series A, Containing Papers of a Mathematical and Physical Character* 142.846 (1933), pp. 1–25. DOI: 10.1098/rspa.1933.0152. eprint: https://royalsocietypublishing.org/doi/pdf/10.1098/rspa.1933.0152. URL: https://royalsocietypublishing.org/doi/abs/10.1098/rspa.1933.0152.

[5] B. P. Abbott and others. "GW170817: Observation of Gravitational Waves from a Binary Neutron Star Inspiral". In: *Phys. Rev. Lett.* 119 (16 Oct. 2017), p. 161101. DOI: 10.1103/PhysRevLett.119.161101. URL: https://link.aps.org/doi/10.1103/PhysRevLett.119.161101.

[6] B. Pontecorvo. "Mesonium and Antimesonium". In: *Soviet Journal of Experimental and Theoretical Physics* 6 (1958), p. 429.

[7] Matthew Gregory Dunkman. "Measurement of Atmospheric Muon Neutrino Disappearance with IceCube-DeepCore". PhD thesis. Penn State U., 2015-05-27. URL: https://etda.libraries.psu.edu/catalog/27226.

[8] P. F. de Salas et al. "Status of neutrino oscillations 2018: 3σ hint for normal mass ordering and improved CP sensitivity". In: *Phys. Lett.* B782 (2018), pp. 633–640. DOI: 10.1016/j.physletb.2018.06.019. arXiv: 1708.01186 [hep-ph].

[9] L. Wolfenstein. "Neutrino oscillations in matter". In: *Phys. Rev. D* 17 (9 May 1978), pp. 2369–2374. DOI: 10.1103/PhysRevD.17.2369. URL: https://link.aps.org/doi/10.1103/PhysRevD.17.2369.

[10] C. L. Cowan et al. "Detection of the Free Neutrino: a Confirmation". In: *Science* 124.3212 (1956), pp. 103–104. ISSN: 0036-8075. DOI: 10.1126/science.124.3212.103. eprint: https://science.sciencemag.org/content/124/3212/103.full.pdf. URL: \url{https://science.sciencemag.org/content/124/3212/103}.

[11] Bruno Pontecorvo. "Report PD-205". Chalk River Laboratory. 1946.

[12] Bruce T. Cleveland et al. "Measurement of the Solar Electron Neutrino Flux with the Homestake Chlorine Detector". In: *The Astrophysical Journal* 496.1 (Mar. 1998), pp. 505–526. DOI: 10.1086/305343. URL: https://doi.org/10.1086%2F305343.

[13] S. Fukuda et al. "The Super-Kamiokande detector". In: *Nuclear Instruments and Methods in Physics Research Section A: Accelerators, Spectrometers, Detectors*

and Associated Equipment 501.2 (2003), pp. 418 –462. ISSN: 0168-9002. DOI: https://doi.org/10.1016/S0168-9002(03)00425-X. URL: http://www.sciencedirect.com/science/article/pii/S016890020300425X.

[14] A. Bellerive et al. "The Sudbury Neutrino Observatory". In: (2016). DOI: 10.1016/j.nuclphysb.2016.04.035. eprint: arXiv:1602.02469.

[15] Juan de Dios Zornoza and Juan Zúñiga. *The ANTARES neutrino telescope*. 2012. eprint: arXiv:1209.6480.

[16] IceCube Collaboration, M. G. Aartsen, et al. "The IceCube Neutrino Observatory: Instrumentation and Online Systems". In: (2016). DOI: 10.1088/1748-0221/12/03/P03012. eprint: arXiv:1612.05093.

[17] F. Bloch. "Zur Bremsung rasch bewegter Teilchen beim Durchgang durch Materie". In: *Annalen der Physik* 408.3 (1933), pp. 285–320. DOI: 10.1002/andp.19334080303. eprint: https://onlinelibrary.wiley.com/doi/pdf/10.1002/andp.19334080303. URL: https://onlinelibrary.wiley.com/doi/abs/10.1002/andp.19334080303.

[18] M. Ackermann et al. "Optical properties of deep glacial ice at the South Pole". In: *Journal of Geophysical Research: Atmospheres* 111.D13 (2006). DOI: 10.1029/2005JD006687. eprint: https://agupubs.onlinelibrary.wiley.com/doi/pdf/10.1029/2005JD006687. URL: https://agupubs.onlinelibrary.wiley.com/doi/abs/10.1029/2005JD006687.

[19] R. Abbasi et al. "The design and performance of IceCube DeepCore". In: *Astroparticle Physics* 35.10 (2012), pp. 615 –624. ISSN: 0927-6505. DOI: https:

//doi.org/10.1016/j.astropartphys.2012.01.004. URL: http://www.sciencedirect.com/science/article/pii/S0927650512000254.

[20]   IceCube Collaboration. *Cosmic Ray Spectrum and Composition from PeV to EeV Using 3 Years of Data From IceTop and IceCube*. 2019. eprint: arXiv:1906.04317.

[21]   Hamamatsu Corp. *R7081-02 Photomultiplier Tube Data (2003)*.

[22]   The IceCube Collaboration. "The IceCube Data Acquisition System: Signal Capture, Digitization, and Timestamping". In: (2008). DOI: 10.1016/j.nima.2009.01.001. eprint: arXiv:0810.4930.

[23]   The IceCube Collaboration. "Calibration and Characterization of the IceCube Photomultiplier Tube". In: (2010). DOI: 10.1016/j.nima.2010.03.102. eprint: arXiv:1002.2442.

[24]   Dmitry Chirkin. "Study of South Pole ice transparency with IceCube flashers". In: *Proceedings of the 32nd International Cosmic Ray Conference, ICRC 2011* 4 (Jan. 2011), pp. 161–. DOI: 10.7529/ICRC2011/V04/0333.

[25]   Rongen, Martin. "Measuring the optical properties of IceCube drill holes". In: *EPJ Web of Conferences* 116 (2016), p. 06011. DOI: 10.1051/epjconf/201611606011. URL: https://doi.org/10.1051/epjconf/201611606011.

[26]   IceCube Collaboration. *Internal HQE Charge Measurement*. 2009. eprint: https://wiki.icecube.wisc.edu/index.php/HighQE_DOM/PMT_measurement.

[27] R. C. Bay et al. "South Pole paleowind from automated synthesis of ice core records". In: *Journal of Geophysical Research: Atmospheres* 115.D14 (2010). DOI: 10.1029/2009JD013741. eprint: https://agupubs.onlinelibrary.wiley.com/doi/pdf/10.1029/2009JD013741. URL: https://agupubs.onlinelibrary.wiley.com/doi/abs/10.1029/2009JD013741.

[28] Nathan Bramall et al. "A deep high-resolution optical log of dust, ash, and stratigraphy in South Pole glacial ice". In: *Geophys. Res. Lett* 32 (Nov. 2005). DOI: 10.1029/2005GL024236.

[29] IceCube Collaboration. "Measurement of South Pole ice transparency with the IceCube LED calibration system". In: (2013). DOI: 10.1016/j.nima.2013.01.054. eprint: arXiv:1301.5361.

[30] Gustav Mie. "Beiträge zur Optik trüber Medien, speziell kolloidaler Metallösungen". In: *Annalen der Physik* 330.3 (1908), pp. 377–445. DOI: 10.1002/andp.19083300302. eprint: https://onlinelibrary.wiley.com/doi/pdf/10.1002/andp.19083300302. URL: https://onlinelibrary.wiley.com/doi/abs/10.1002/andp.19083300302.

[31] Y. D. He and P. B. Price. "Remote sensing of dust in deep ice at the South Pole". In: *Journal of Geophysical Research: Atmospheres* 103.D14 (1998), pp. 17041–17056. DOI: 10.1029/98JD01643. eprint: https://agupubs.onlinelibrary.wiley.com/doi/pdf/10.1029/98JD01643. URL: https://agupubs.onlinelibrary.wiley.com/doi/abs/10.1029/98JD01643.

[32] L. G. Henyey and J. L. Greenstein. "Diffuse radiation in the Galaxy". In: *The Astrophysical Journal* 93 (Jan. 1941), pp. 70–83. DOI: 10.1086/144246.

[33] Dmitry Chirkin. "Evidence of optical anisotropy of the South Pole ice". In: *Proceedings, 33rd International Cosmic Ray Conference (ICRC2013): Rio de Janeiro, Brazil, July 2-9, 2013*, p. 0580. URL: http://www.cbpf.br/%7Eicrc2013/papers/icrc2013-0580.pdf.

[34] IceCube Collaboration et al. "First observation of PeV-energy neutrinos with IceCube". In: (2013). DOI: 10.1103/PhysRevLett.111.021103. eprint: arXiv:1304.5356.

[35] Abhik Jash. "Studies on the Physics of Resistive Plate Chambers in Relation to the INO Experiment". PhD thesis. Apr. 2018.

[36] IceCube Collaboration et al. "Neutrinos and Cosmic Rays Observed by IceCube". In: (2017). DOI: 10.1016/j.asr.2017.05.030. eprint: arXiv:1701.03731.

[37] The IceCube et al. "Multi-messenger observations of a flaring blazar coincident with high-energy neutrino IceCube-170922A". In: (2018). DOI: 10.1126/science.aat1378. eprint: arXiv:1807.08816.

[38] IceCube Collaboration, M. G. Aartsen, et al. "Evidence for High-Energy Extraterrestrial Neutrinos at the IceCube Detector". In: (2013). DOI: 10.1126/science.1242856. eprint: arXiv:1311.5238.

[39] IceCube Collaboration, M. G. Aartsen, et al. "A combined maximum-likelihood analysis of the high-energy astrophysical neutrino flux measured with IceCube". In: (2015). DOI: 10.1088/0004-637X/809/1/98. eprint: arXiv:1507.03991.

[40] IceCube Collaboration. "Energy Reconstruction Methods in the IceCube Neutrino Telescope". In: (2013). DOI: 10.1088/1748-0221/9/03/P03009. eprint: arXiv:1311.4767.

[41] IceCube Collaboration. *The IceCube Neutrino Observatory - Contributions to ICRC 2017 Part II: Properties of the Atmospheric and Astrophysical Neutrino Flux*. 2017. eprint: arXiv:1710.01191.

[42] IceCube Collaboration. "Measurement of Atmospheric Neutrino Oscillations at 6-56 GeV with IceCube DeepCore". In: (2017). DOI: 10.1103/PhysRevLett.120.071801. eprint: arXiv:1707.07081.

[43] Spencer Axani. "SPE Fitting". In: *IceCube Internal Resource* (). URL: https://wiki.icecube.wisc.edu/index.php/SPE_Fitting.

[44] *Signal Simulation Metadata*. https://grid.icecube.wisc.edu/simulation/dataset/12359. Accessed: 2019-07-18.

[45] D. Heck et al. "CORSIKA: A Monte Carlo code to simulate extensive air showers". In: (1998).

[46] *dCorsika*. https://wiki.icecube.wisc.edu/index.php/DCorsika_releases. Accessed: 2019-07-18.

[47] Dmitry Chirkin. "dCORSIKAupdate". In: *IceCube Internal Report* (). URL: https://icecube.wisc.edu/~dima/work/BKP/DCS/REPORT8/paper.pdf.

[48] Dmitry Chirkin. "Fluxes of atmospheric leptons at 600-GeV - 60-TeV". In: (2004). arXiv: hep-ph/0407078 [hep-ph].

[49] *Corsika*. http://software.icecube.wisc.edu/documentation/projects/simprod-scripts/modules/corsika.html. Accessed: 2019-07-18.

[50] J. R. Hoerandel. "On the knee in the energy spectrum of cosmic rays". In: (2002). DOI: 10.1016/S0927-6505(02)00198-6. eprint: arXiv:astro-ph/0210453.

[51] J.-H. Koehne et al. "PROPOSAL: A tool for propagation of charged leptons". In: *Computer Physics Communications* 184.9 (2013), pp. 2070 –2090. ISSN: 0010-4655. DOI: https://doi.org/10.1016/j.cpc.2013.04.001. URL: http://www.sciencedirect.com/science/article/pii/S0010465513001355.

[52] Claudio Kopper. *CLSim GitHub*. https://github.com/claudiok/clsim. Accessed: 2019-07-18.

[53] S. Agostinelli et al. "Geant4—a simulation toolkit". In: *Nuclear Instruments and Methods in Physics Research Section A: Accelerators, Spectrometers, Detectors and Associated Equipment* 506.3 (2003), pp. 250 –303. ISSN: 0168-9002. DOI: https://doi.org/10.1016/S0168-9002(03)01368-8. URL: http://www.sciencedirect.com/science/article/pii/S0168900203013688.

[54] Claudio Kopper. *CLSim Procedure*. http://software.icecube.wisc.edu/documentation/projects/clsim/overview.html#light-source-to-steps. Accessed: 2019-07-18.

[55] *Background Simulation Metadata*. https://grid.icecube.wisc.edu/simulation/dataset/12531. Accessed: 2019-07-18.

[56] *Polyplopia*. http://software.icecube.wisc.edu/documentation/projects/polyplopia/index.html. Accessed: 2019-07-18.

[57] *Pmt-Simulator*. https://wiki.icecube.wisc.edu/index.php/Pmt-simulator. Accessed: 2019-07-18.

[58] M. J. Larson. "Simulation and identification of non-Poissonian noise triggers in the IceCube neutrino detector". PhD thesis. Alabama U., 2013. URL: https://ir.ua.edu/handle/123456789/1927.

[59] Michelangelo D'Agostino. "Effective Livetime For Weighted Corsika". In: *IceCube Internal Report* (2009). URL: https://internal-apps.icecube.wisc.edu/reports/data/icecube/2009/02/001/icecube_200902001_v2.pdf.

[60] IceCube Collaboration. *Internal SLC hit cleaning*. 2010. eprint: https://wiki.icecube.wisc.edu/index.php/SLC_hit_cleaning\#SeededRTCleaning_with_pulses.

[61] Donald E. Groom, Nikolai V. Mokhov, and Sergei I. Striganov. "Muon stopping power and range tables 10-MeV to 100-TeV". In: *Atom. Data Nucl. Data Tabl.* 78 (2001), pp. 183–356. DOI: 10.1006/adnd.2001.0861.

[62] *LineFit*. http://software.icecube.wisc.edu/documentation/projects/linefit/index.html. Accessed: 2019-07-18.

[63] The AMANDA Collaboration, J. Ahrens, et al. "Muon Track Reconstruction and Data Selection Techniques in AMANDA". In: (2004). DOI: 10.1016/j.nima.2004.01.065. eprint: arXiv:astro-ph/0407044.

[64] N. van Eijndhoven, O. Fadiran, and G. Japaridze. "Implementation of a Gauss convoluted Pandel PDF for track reconstruction in Neutrino Telescopes". In: (2007). DOI: `10.1016/j.astropartphys.2007.09.001`. eprint: `arXiv:0704.1706`.

[65] George Japaridze and Mathieu Ribordy. "Realistic arrival time distribution from an isotropic light source". In: (2005). arXiv: `astro-ph/0506136 [astro-ph]`.

[66] N. van Eijndhoven, O. Fadiran, and G. Japaridze. "Implementation of a Gauss convoluted Pandel PDF for track reconstruction in neutrino telescopes". In: *Astroparticle Physics* 28.4 (2007), pp. 456 –462. ISSN: 0927-6505. DOI: `https://doi.org/10.1016/j.astropartphys.2007.09.001`. URL: `http://www.sciencedirect.com/science/article/pii/S0927650507001260`.

[67] *FiniteReco*. `http://software.icecube.wisc.edu/documentation/projects/finiteReco/index.html`. Accessed: 2019-07-18.

[68] J. Feintzeig. "Searches for Point-like Sources of Astrophysical Neutrinos with the IceCube Neutrino Observatory". PhD thesis. The University of Wisconsin - Madison, 2014.

[69] IceCube Collaboration, M. G. Aartsen, et al. "Characterization of the Atmospheric Muon Flux in IceCube". In: (2015). DOI: `10.1016/j.astropartphys.2016.01.006`. eprint: `arXiv:1506.07981`.

[70] Kesar Singh and Minge Xie. "Bootstrap : A Statistical Method". In: 2008.

[71] Glen Cowan. "Error analysis with weighted events". In: (2014). URL: `https://www.pp.rhul.ac.uk/~cowan/stat/notes/errors_with_weights.pdf`.

[72] Chris Wendt. "Afterpulse Data". In: *Internal Afterpulse Measurements* (). URL: https://icecube.wisc.edu/~chwendt/afterpulse-notes/.